POLARITY DRIVEN LAMINAR PATTERN FORMATION BY LATERAL-INHIBITION IN 2D AND 3D BILAYER GEOMETRIES

JOSHUA W. MOORE[1], TREVOR C. DALE[2], AND THOMAS E. WOOLLEY[1]

Abstract. Fine-grain patterns produced by juxtacrine signalling, have previously been studied using static monolayers as cellular domains. However, analytic results are usually restricted to a few cells due to the algebraic complexity of nonlinear dynamical systems. Motivated by concentric patterning of Notch expression observed in the mammary gland, we combine concepts from graph and control theory to represent cellular connectivity and behaviour. The resulting theoretical framework allows us to exploit the symmetry of multicellular bilayer structures in 2D and 3D, thereby deriving analytical conditions that drive the dynamical system to form laminar patterns, consistent with the formation of cell polarity by activator localisation. Critically, the patterning conditions are independent of the precise dynamical details, thus the framework allows for generality in understanding the influence of cellular geometry and signal polarity on patterning using lateral-inhibition systems. Applying the analytic conditions to mammary organoids suggests that intense cell signalling polarity is required for the maintenance of stratified cell types within a static bilayer using a lateral-inhibition mechanism. Furthermore, by employing 2D and 3D cell-based models, we highlight that the cellular polarity conditions derived from static domains can generate laminar patterning in dynamic environments. However, they are insufficient for the maintenance of patterning when subjected to substantial morphological perturbations. In agreement with the mathematical implications of strict signalling polarity induced on the cells, we propose an adhesion-dependent Notch-Delta biological process that has the potential to initiate bilayer stratification in a developing mammary organoid.

Keywords: Pattern formation, Nonlinear systems, Lateral-inhibition, Bilayer structures, Mammary organoids, Notch

1. Introduction

Lateral-inhibition is considered a fundamental driving process for the emergence of fine-grain pattern formation in tissues [1]. At the resolution of the tissue, lateral-inhibition is the process in which the activation of a cell is inhibited by the increased activity in neighbouring cells thereby preventing each other from converging the same activity state [1]. The resultant fine-grain patterns are critical in the development of many multicellular biological systems such as *Drosophila* eye formation, murine hair organisation in

[1]School of Mathematics, Cardiff University, Senghennydd Rd, Cardiff, CF24 4AG, UK

[2]School of Biosciences, Cardiff University, Museum Ave, Cardiff, CF10 3AX, UK

E-mail addresses: moorej16@cardiff.ac.uk.

auditory epithelia and establishing blood vessels during human embryogenesis [2–4]. In contrast to the approach of using reaction-diffusion systems that consider diffusive activator proteins over different signal ranges to generate spatially continuous patterns [5, 6], systems of ordinary differential equations (ODEs) can be used to generate a discretised description of the space, enabling the formation of fine-grain patterns at the resolution of individual cells. These spatially discrete ODE systems seek to emulate the behaviour of contact-dependent cell-cell non-diffusive signalling mechanism known as juxtacrine signalling, a common form of cellular communication in epithelial tissue [1].

The juxtacrine signalling mechanism relies on membrane-bound signal proteins on a sender cell binding to surface anchored receptors on a receiving cell, imposing a contact-dependence [1]. Critically, cells can only use juxtacrine signalling to communicate with their direct neighbours in the absence of activator/receptor extensions [7], as demonstrated in Figure 1a. Consequently, the spatial organisation of cells is of fundamental importance in orchestrating signal protein patterning required for specific organ development [8].

Mathematically, juxtacrine signalling dependent pattern formation has been extensively studied over the last two decades [7, 11–14], commonly focusing on lateral-inhibition mechanisms. An overarching conclusion from the family of studies focused on juxtacrine pattern analysis of lateral-inhibition models is that linear analysis techniques in isolation are insufficient to determine precise conditions for patterning, and are only able to predict the existence of patterning [11]. In light of this, there has been a reliance on numerical simulations to elucidate parameter regimes in which patterns occur.

However, the model parameters are not the only factors influencing the emergence of patterns. The geometry of the cellular domain on which the juxtacrine model is being applied has a large impact on the obtainable patterning. This was highlighted by Webb et al. (2004), where they compared a honeycomb domain to a simple grid domain in 2D under a standard four-point connectivity stencil for cellular connectivity (see Figure 2 and Figure 6a). In doing so, they show the considerable differences in parameter regimes required to achieve similar patterns in different domain types [13]. The underlying features kinetics that describe a lateral-inhibition model imply that adjacent cells do not converge to similar steady states, thus generating salt-and-pepper type patterns Figure 2 [10]. Although, asymmetries in cellular geometry have the capacity to produce unique patterning that are unobtainable on regular domains but are more biologically realistic, namely clusters of cells with similar steady states [12]. In support of this, when coupling a mechanism for cellular protrusions with a lateral-inhibition spatially discrete ODE system, a large family of distinct patterns were observed over a regular 2D honeycomb spatial domain, specifically, the generation of laminar patterns whereby the tissue converged to rows of alternating activity (Figure 2c) [7]. Such laminar patterns driven by lateral-inhibition mechanisms have been observed in various biological systems such as in the mammary gland and zebrafish skin pigments [15, 16]. Though, to achieve laminar patterns using the lateral-inhibition

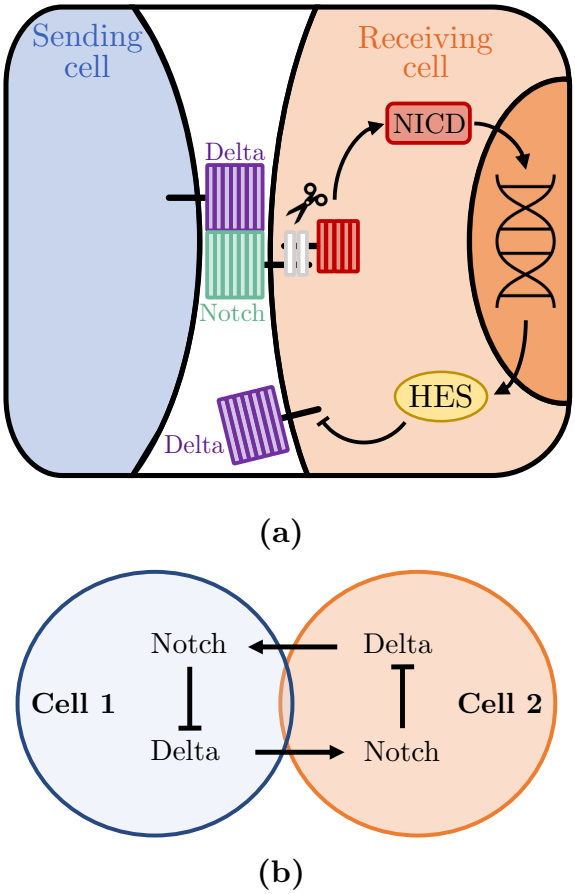

FIGURE 1. A schematic diagram of the canonical Notch pathway as an example juxtacrine signalling mechanism. (a) Membrane-bound Delta ligands (purple rectangles) on a signal sending cell bind to membrane-bound Notch receptors (green rectangles) on a receiving cell. The activation of Notch receptors initiates the cleavage of Notch into the cytosol of the receiving cell, known as NICD. The NICD then translocates to the nucleus where it promotes the transcription of HES, an inhibitor of Delta ligand targets. Adapted from [9]. (b) A minimal representation of the negative feedback dynamics of Notch and Delta in coupled cells. This mathematical simplification was first conceived in [10].

model, the authors conclude cellular protrusions must be preferentially directed perpendicular to the active row of cells to ensure contact with the inactivate cells to maintain their activity [7]. These results suggest the existence of planar cell polarity (denoted by polarity herein) of cell-cell receptors and/or activators in the absence of cellular protrusions to generate laminar patterns using a lateral-inhibition mechanism.

An alternative approach to pattern formation analysis in lateral-inhibition models was introduced by [17], where they considered cells as vertices on a connected graph that interact using dynamic input-output systems, known as interconnected dynamical systems. Namely, interconnected dynamical systems are constructed from coupling ODE subsystems using networks, whereby the internal kinetics are embedded within each node. This approach produced analytic conditions for the existence and stability of checkerboard patterning in cyclic domains, independent of the number of cells, as demonstrated in Figure 2, thus, extending

the analysis conducted in [11–13] that was restricted to only two cells due to the complexity of the systems studied.

Moreover, the graph-theoretic approach to juxtacrine systems was later refined when graph partitioning was applied to represent patterning within collections of cells [18], generalising the previous results of [17], which developed a framework to prove the existence and stability of a family of patterns within periodic domains in both grid and hexagonal lattices. These studies emphasise the relationship between how cells are connected and the obtainable patterns.

Nonetheless, these conditions were derived using static domains and were heavily dependent on several assumptions regarding the graph's topology (reviewed in Section 2.3). These assumptions cannot always be adhered to when investigating patterning on an evolving biological system, although they may be true in certain quasi-steady stages of its development where static cellular geometries may be applicable.

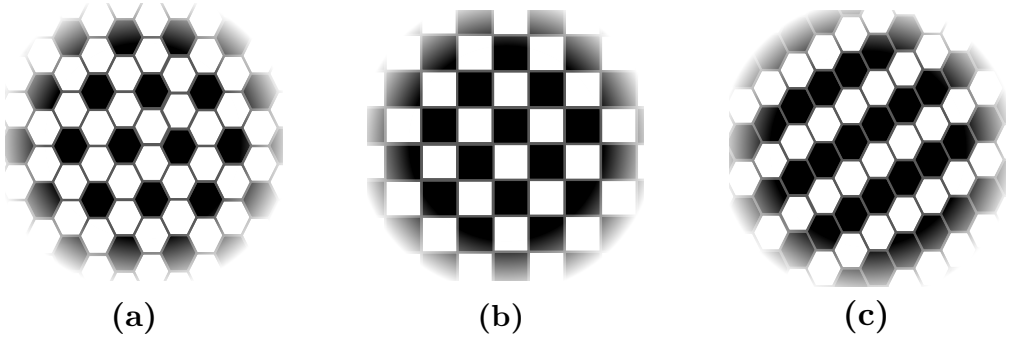

FIGURE 2. Activation patterns by lateral-inhibition mechanisms in hexagonal and grid lattices. Salt-and-pepper patterns formed by lateral-inhibition in over a (a) hexagonal and (b) grid cellular domains as demonstrated in [10]. An idealisation of the laminar patterns produced in [7] by coupling active row perpendicular cellular protrusions to lateral-inhibition mechanism over a hexagonal cellular domain.

The canonical Notch pathway is a well-studied example of a juxtacrine signalling pathway with an essential role in cell fate determination and morphological bifurcations in developmental systems [15, 19–21]. The Notch pathway describes a lateral-inhibition mechanism between neighbouring cells, whereby the activation of the Notch receptor via membrane-anchored Delta ligands on adjacent cells leads to the accumulation of Notch-intracellular-domain (NICD) within the cytosol. The build-up of NICD leads to the transcription of members of the Hair-Enhancer of Split (HES) superfamily, which acts as an inhibitor of the target genes that promote the downstream production of Delta ligands and lineage-specific gene repressor [22]. That is, the activation of Notch leads to the inactivation of Delta within the same cell as shown in see Figure 1a. Mammals exhibit four paralogues of the Notch receptor, Notch1 to Notch4, each with associated Delta-like ligands that each observe the autoregulation mechanism outlined by the canonical pathway [22]. A detailed description of the canonical Notch pathway can be found elsewhere [9].

A particular biological system that is highly dependent on the Notch pathway is the mammary organoid. Mammary organoids are three-dimensional tissue cultures that are currently the most accurate representation of *in vivo* mammary gland biology [23]. Throughout its development, the mammary organoid retains a consistent bilayer structure of cells as seen in Figure 3. That is, the outer layer holds the elongated, contractile basal cells, whereas the inner layer consists of cuboidal luminal cells. Once these layers have been established, a hollow lumen forms, surrounded by the bilayer of cells.

Notch1 signalling (denoted by Notch signalling hereafter) is a critical determinant of luminal cell differentiation in mammary epithelial cells (MECs) [15]. It has been established that Notch activation is required to support differentiation of the basal stem cells to the luminal population in the mammary organoid and therefore it is a key component in the maintenance of a developing mammary system [24]. In addition, sudden Notch activation within the basal coincides with the locations of symmetry-breaking events of embryonic MECs [15]. Thus, it has been hypothesised that Notch activation via basal cells, or contact with the basement membrane, is required to develop branched epithelia [22].

During any stage of development of the mammary gland and organoid, MECs are capable of self-organising to form an outer layer of cells that highly express Delta (low Notch), and in contrast, inner layers of cells that surround a hollow lumen that expresses low Delta (high Notch), see Figures 3b-3d [24, 25]. It is unclear whether this spatial patterning is a consequence or cause of the morphology of developing mammary ducts, although, it is clear that the concentric (laminar) patterning of the bilayer of cells is robust to morphological perturbations. Critically, the observed laminar patterning of Notch expression in the mammary gland cannot be achieved by the canonical intracellular lateral-inhibition mechanism in isolation [7, 24], which suggests an intercellular intervention in signal transfer. Specifically, we investigate the existence of activator polarity for the emergence of laminar pattern formation of Notch using a lateral-inhibition mechanism in the distinct mammary cellular domains.

Conditions defining laminar pattern formation in bilayer geometries using a simple mathematical lateral-inhibition model concerning activator anisotropy have yet to be derived. Here, we apply the general interconnected systems framework to a previously developed ODE model of Notch-Delta and obtain conditions on Delta cell-cell transmission that are sufficient for the bilayer laminar patterns to form in agreement with experimental observations. Specifically, we induce activator polarity within each cell by introducing cell-type dependent edge weights to the graph representing cellular connectivity, thus describing the signal anisotropy within the network of cells. Using the cell type-dependent connectivity framework, we analyse the interplay of cellular neighbourhood composition and activator polarity, independent of precise intracellular kinetics and physical dimension, for the instability of the homogeneous steady state of the large-scale dynamical system.

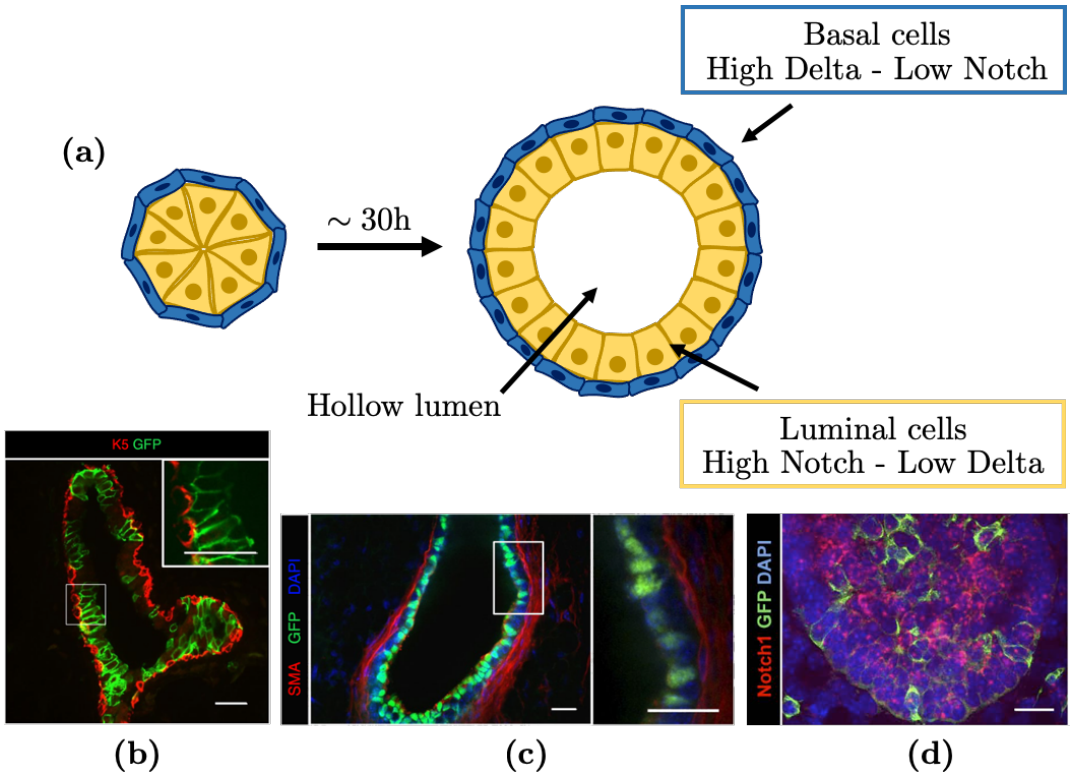

FIGURE 3. The structure of a mammary organoid and the spatial distribution of Notch expression. (a) A simple 2D diagram of the structure of a developing mammary organoid, highlighting lumen formation and maintenance of stratified bilayer. (b-c) Cross-sections of mammary ducts of 6-week old mice, where Notch1-derived lineages are labelled in green by (b) membrane-bound green fluorescent protein (GFP) and (c) nuclear GFP. (d) Representative sections of embryonic mammary buds. The small red dots highlight the presence of Notch1 protein which are clustered towards the centre of the bud. Scale bar, 20μm (10μm in magnifications). Images used with permission from Springer Nature and originally printed in [15].

From properties of monotone dynamical systems, the instability of the homogeneous steady state ensures the existence of pattern formation for the given bilayer template. We then demonstrate the applicability and limitations of the analytic activator ligand polarity conditions for static domains to developing dynamic cellular networks, highlighting the requirement of adaptive control mechanisms for pattern preservation in stochastic connectivity graphs.

The study is structured as follows. In Section 2.1 we start with a classical ODE system used to study cell-cell interactions and then demonstrate how to recast such kinetics as an interconnected dynamical system using regular connected graphs in Section 2.2. In Section 2.3 we describe methods of graph partitioning for large-scale system reduction that preserve global connectivity properties. Next, in Section 2.4, we review the literature from interconnected dynamical systems that we apply in this study, particularly outlining the results that allow us to derive analytic conditions on cell-type dependent weightings of Delta cell-cell transmission. In

Section 3 we predict the existence and stability of laminar patterns in regular bilayer structures by exploiting existing results in graph theory, monotone systems and control theory [17, 18]. We apply the analytic conditions to mammary organoids in Section 4.1 using a Notch-Delta model (NDM), thereby employing a family of fixed regular 2D and 3D structures to investigate the role of local neighbourhood composition on laminar pattern formation. Finally, in Section 4.2, we use 2D and 3D cell-based modelling to highlight the applicability and limitations of the static domains in pattern analysis of developing systems. Critically, we show how the transient transitions of cellular connectivity in a lattice-free dynamic domain can prevent robust pattern formation when considering only signal polarisation as a control mechanism.

2. Interconnected ODE systems for multicellular pattern formation by lateral-inhibition

In this section, we define a framework to investigate the interplay of domain geometry and cellular signalling polarity in laminar pattern formation. To elucidate the dependence of cell-type transmission of Delta in bilayer structures we consider the original lateral-inhibition ODE model constructed in [10]. By adapting the spatial averaging term to include cell-type dependent weightings on Delta transmission to represent cellular polarity, we impose signal transfer anisotropy within the cellular system to promote bilayer laminar pattern formation of Notch-Delta that are experimentally observed (Figures 3b-3d).

In addition, we introduce the notion of the graphical representation of cellular connectivity and a framework for cellular coupling. We later introduce and review the properties of the interconnected ODE system and its associated graph that are used in pattern analysis for lateral-inhibition mechanisms.

2.1. **A model of intercellular lateral-inhibition dynamics.**

The spatially discrete NDM developed by Collier et al. (1996) was the first explicit lateral-inhibition model that was used to investigate fine-grain patterns that are observed in a variety of biological systems [10]. The intracellular kinetics contains only two components, Notch (N) and Delta (D) activation, simplifying the underlying biochemical processes, which allows freedom of interpretation of N and D. When studying the dynamics of Notch-Delta in the mammary organoid, we will consider N to be the NICD active protein concentration within the cytosol and D to be the amount of active membrane-bound Delta ligands on the surface of the cell, see Figure 1a. The inverse relationship between intracellular Notch and Delta is the key feature of the spatially discrete ODE model, which is described by the negative feedback loop depicted in Figure 1b and thus is characterised by the following assumptions:

(i) Cells interact through Delta-Notch signalling only with cells with which they are in direct contact, that is, adhering to the juxtacrine mechanism.

(ii) The rate of production of Notch activity is an increasing function of the level of Delta activity in neighbouring cells.

(iii) The rate of production of Delta activity is a decreasing function of the level of activated Notch in the same cell.

(iv) Production of Notch and Delta activity is balanced by decay, described by a simple exponential decay with fixed-rate constants.

(v) The activity of Notch and Delta are uniformly distributed throughout the cell.

(vi) Instantaneous transcription of downstream Notch targets such that the model assumes no delay in Notch and Delta interactions.

These assumptions outline the Notch-Delta lateral-inhibition model, which can be formalised mathematically as,

$$\dot{N}_i = \underbrace{f\left(\langle D_i \rangle\right)}_{\substack{\text{NICD activation via} \\ \text{Delta binding from} \\ \text{adjacent cells}}} - \underbrace{\mu_1 N_i}_{\substack{\text{NICD} \\ \text{degradation}}}, \tag{2.1}$$

$$\dot{D}_i = \underbrace{g\left(N_i\right)}_{\substack{\text{Delta inhibition} \\ \text{by NICD}}} - \underbrace{\mu_2 D_i}_{\substack{\text{Delta} \\ \text{degradation}}}, \tag{2.2}$$

where f and g are bounded increasing and decreasing functions respectively. These functions have the form,

$$f(x) = \frac{x^k}{a + x^r} \quad \text{and} \quad g(x) = \frac{1}{1 + bx^s}, \tag{2.3}$$

where parameters $a, b, \mu_1, \mu_2 > 0$ and Hill coefficients $r, s \geq 1$. The subscript i corresponds to cell identity within the system and the definition of the local spatial mechanism, $\langle D_i \rangle$, will be discussed in Section 2.2 in order to embed the NDM (2.1-2.2) system into a network of cells.

2.2. **A network approach to cellular connectivity with signal anisotropy.**

To recast the NDM (2.1-2.2) as an interconnected dynamical system we represent the cellular connections as an undirected connected N_c-regular graph $\mathcal{G} = \mathcal{G}(V, E)$, where vertices $v \in V$ represent cells and edges $e \in E$ correspond to cellular connections, see Figure 4. The vertices v_i and v_j representing cells i and j are considered to be connected if there exists an edge, $e_{i,j}$, between v_i and v_j such that $e_{i,j} \neq \emptyset$. Physically, we say that $e_{i,j} \neq \emptyset$ if the cell membranes of cell i and j are in contact. We represent the signal strength of cellular connectivity between cells i and j using nonnegative cell-type dependent weighting coefficients $w_{i,j}$. Namely,

$$w_{i,j} = \begin{cases} w_1 & \text{if } e_{i,j} \neq \emptyset \wedge \tau_i = \tau_j, \\ w_2 & \text{if } e_{i,j} \neq \emptyset \wedge \tau_i \neq \tau_j, \\ 0 & \text{if } e_{i,j} = \emptyset, \end{cases} \tag{2.4}$$

where $w_1, w_2 \in \mathbb{R}_{>0}$ and cell-type of cell i is denoted by τ_i. Explicitly, $w_{i,j} = 0$ if cells i and j are not connected. If cells i and j are connected and of the same type, $w_{i,j} = w_1$, and if cells i and j are connected and are different types then $w_{i,j} = w_2$, as highlighted in Figure 4.

As we consider an undirected graph from we have that $w_{i,j} = w_{j,i}$, namely, we consider cells to be connected if cell membranes are in contact and therefore there is a connectivity symmetry between any two connected cells. The coefficients $w_{i,j}$ can be used to mediate Delta transmission between adjacent cells dependent on cell-type inducing a membrane activator anisotropy within the cellular connectivity graph and thus $w_{i,j}$ will be the focus of our study.

We introduce graph cellular connectivity to the NDM (2.1-2.2) using the associated weighted adjacency matrix of $\mathcal{G}$. We consider a system of $\mathcal{N}$ cells such that $\mathcal{N} \in \{2n : n \in \mathbb{N}\}$ to account for bilayer regular structures. Then the weighted adjacency matrix of $\mathcal{G}$ is defined by $[w_{i,j}] = \boldsymbol{W} \in \mathbb{R}_{\geq 0}^{\mathcal{N}\times\mathcal{N}}$ as in [17, 18], where we have included cell-type dependent edge weights here. To represent the cell-type stratified bilayer structures of the mammary gland, we consider two cell types, basal and luminal cells, which are organised into separate layers of the tissue as seen in Figure 3a. As $\mathcal{G}$ is an undirected connected N_c-regular graphs, we are assuming the lattice structures representing cellular connectivity are symmetric with respect to each layer and have periodic boundaries in 2D and 3D. Critically, the both of these properties are induced by the regularity of the graph, that is, each vertex is equipped with the number of edges and associated weights. Following from the bilayer structure of the graph $\mathcal{G}$, the associated weighted adjacency matrix $\boldsymbol{W}$ can be constructed from the matrices $\boldsymbol{W}_1, \boldsymbol{W}_2 \in \mathbb{R}_{\geq 0}^{(\mathcal{N}/2)\times(\mathcal{N}/2)}$. Namely, $\boldsymbol{W}$ has the following form,

$$\boldsymbol{W} = \begin{bmatrix} \boldsymbol{W}_1 & \boldsymbol{W}_2 \\ \boldsymbol{W}_2 & \boldsymbol{W}_1 \end{bmatrix}. \tag{2.5}$$

Here row i of $\boldsymbol{W}_1$ represents the cellular connections of cell i to adjacent cells of the same type, and the rows of $\boldsymbol{W}_2$ correspond to the cellular connections to cells of differing types where cells are numbered 1 to $\mathcal{N}/2$ in the basal layer and $\mathcal{N}/2 + 1$ to $\mathcal{N}$ in the luminal layer as in shown in Figure 4 in terms of Delta transfer between cells. For example, for the standard orthogonal template for a bilayer of cells given in Figure 4, has

connectivity matrices,

$$\boldsymbol{W}_1 = w_1 \begin{bmatrix} 0 & 1 & 0 & 0 & \cdots & 0 & 1 \\ 1 & 0 & 1 & 0 & \cdots & 0 & 0 \\ 0 & 1 & 0 & 1 & 0 & \cdots & 0 \\ \vdots & \ddots & \ddots & \ddots & \ddots & \ddots & \vdots \\ 0 & \cdots & 0 & 1 & 0 & 1 & 0 \\ 0 & 0 & \cdots & 0 & 1 & 0 & 1 \\ 1 & 0 & \cdots & 0 & 0 & 1 & 0 \end{bmatrix} \quad \text{and} \quad \boldsymbol{W}_2 = w_2 \boldsymbol{I}_{\mathcal{N}/2}, \tag{2.6}$$

where $\boldsymbol{I}_{\mathcal{N}/2}$ is the $(\mathcal{N}/2) \times (\mathcal{N}/2)$ identity matrix.

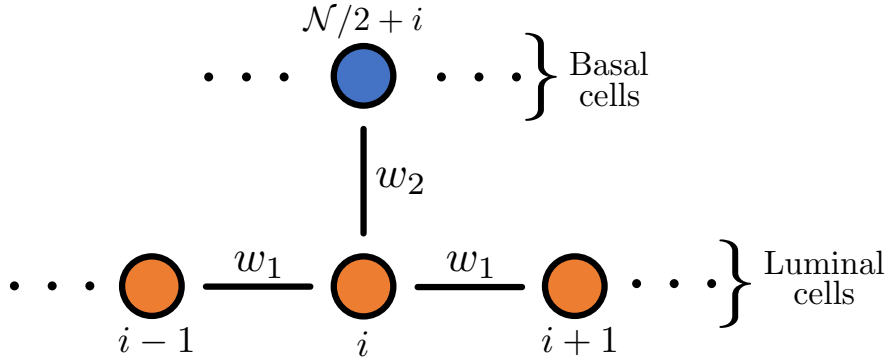

FIGURE 4. An illustrative computational template for cell-type dependent weighted graph structure of a bilayer $\mathcal{N}$ cells. We consider the edge structure from the perspective of cell i within a bilayer graph of luminal and basal cell types. The edge weights w_1 and w_2 determine the strength of connectivity between cells of the same and different types, respectively.

The network representation of cellular connectivity is introduced to the NDM (2.1-2.2) via the averaging operator $\langle \cdot \rangle$. Explicitly, cell-type dependent Delta transmission between adjacent cells in static geometries is described by

$$\langle \boldsymbol{D}(t) \rangle = \frac{1}{n_1 w_1 + n_2 w_2} \boldsymbol{W} \boldsymbol{D}(t), \tag{2.7}$$

where $\boldsymbol{D}(t)$ represents a vector of Delta concentrations for each cell in the system, $\boldsymbol{D}(t) = [D_1(t), ..., D_N(t)]^T$. The value n_1 corresponds to the number of cells of the same type adjacent to cell i, whereas n_2 is the number of cells adjacent of a different type, such that $N_c = n_1 + n_2$, for example, $n_1 = 2$ and $n_2 = 1$ in Figure 4. In addition, we introduce notation for the total scale weighting for each cell, $N_w = n_1 w_1 + n_2 w_2$, for brevity. The inclusion of the scaling term preserves the averaging process that is assumed for the spatially well-mixed NDM (2.1-2.2) (assumption (v)) [10], and also enables the direct comparison of cellular connectivity to a probability transition matrix of a reversible Markov chain, such that in each row $(1/N_w) \sum_j w_{i,j} = 1$ for all i as previously discussed in [17]. Each node within the network is now equipped with the lateral-inhibition

dynamics, which defines a large-scale dynamical system composed of topologically connected subsystems, thus, the establishment of equation (2.7) recasts the NDM (2.1-2.2) as an interconnected dynamical system.

By representing cells as vertices in the connected graph $\mathcal{G}$, we can manipulate the geometry of the graph to investigate parameter regimes of w_1 and w_2 producing an edge weight anisotropy, such that we obtain the desired patterning. Here, we explore a variety of regular periodic (cyclic) fixed lattices 2D and 3D to generate graphs that are shown in Figure 5. We assume that $e_{i,j} \neq \emptyset$ if cell j lies within a circle (or sphere) of radius ρ_c drawn around cell i where the rest length of the lattice is unitary. The circle (or sphere) can be viewed as the cell membrane to which the Notch receptors and Delta ligands are anchored. In addition, we introduce notation for the cell-type ratio for each cell, which is defined as,

$$R_\tau = \frac{\#\text{ of adjacent cells of the same cell-type}}{\#\text{ of adjacent cells of a different cell-type}} = \frac{n_1}{n_2}, \tag{2.8}$$

due to the symmetry of the domains (regular undirected graphs), R_τ is homogeneous for all cells in the system. We chose three representative lattice structures in this study: (1) grid, (2) triangulated and (3) overlapped grid, to characterise the quasi-steady cellular configurations that may occur during the development mammary organoids. We then increase the connectivity radius, ρ_c, to obtain different neighbourhoods around each cell.

For example, when considering a unitary grid lattice, we examine two common cellular neighbourhoods used within the field of Cellular Automata [26]. That is, taking $\rho_c = 1$ yields a Von Neumann neighbourhood, which is defined by a central node, surrounded by 4 other nodes in the north, east, south and west directions (Figure 6a) [27]. Whereas increasing the connectivity spheres radius such that $\rho_c = \sqrt{2}$, we obtain a Moore neighbourhood, that includes the diagonal nodes missing from the Von Neumann neighbourhood (Figure 6b) [27].

Illustrations of the various 2D and 3D bilayer geometries used considered in both analytical and numerical investigations for laminar pattern formation in mammary organoids is given in Figure 5 with a summary of the graph properties given in Table 1.

Lattice type	Connectivity radius, ρ_c	Cellular connectivity, N_c	Cell-type ratio, R_τ
2D Von Neumann (2DVN)	1	3	2
2D Triangulated (2DT)	1	4	1
2D Moore (2DM)	$\sqrt{2}$	5	2/3
3D Von Neumann (3DVM)	1	5	4
3D Overlapped (3DO1)	1	8	1
3D Triangulated (3DT)	1	9	2
3D Overlapped (3DO2)	$\sqrt{2}$	12	2
3D Moore (3DM)	$\sqrt{2}$	13	8/5

TABLE 1. A summary of the lattice geometries in 2D and 3D that can be found in Figure 5 outlining the cellular neighbourhoods.

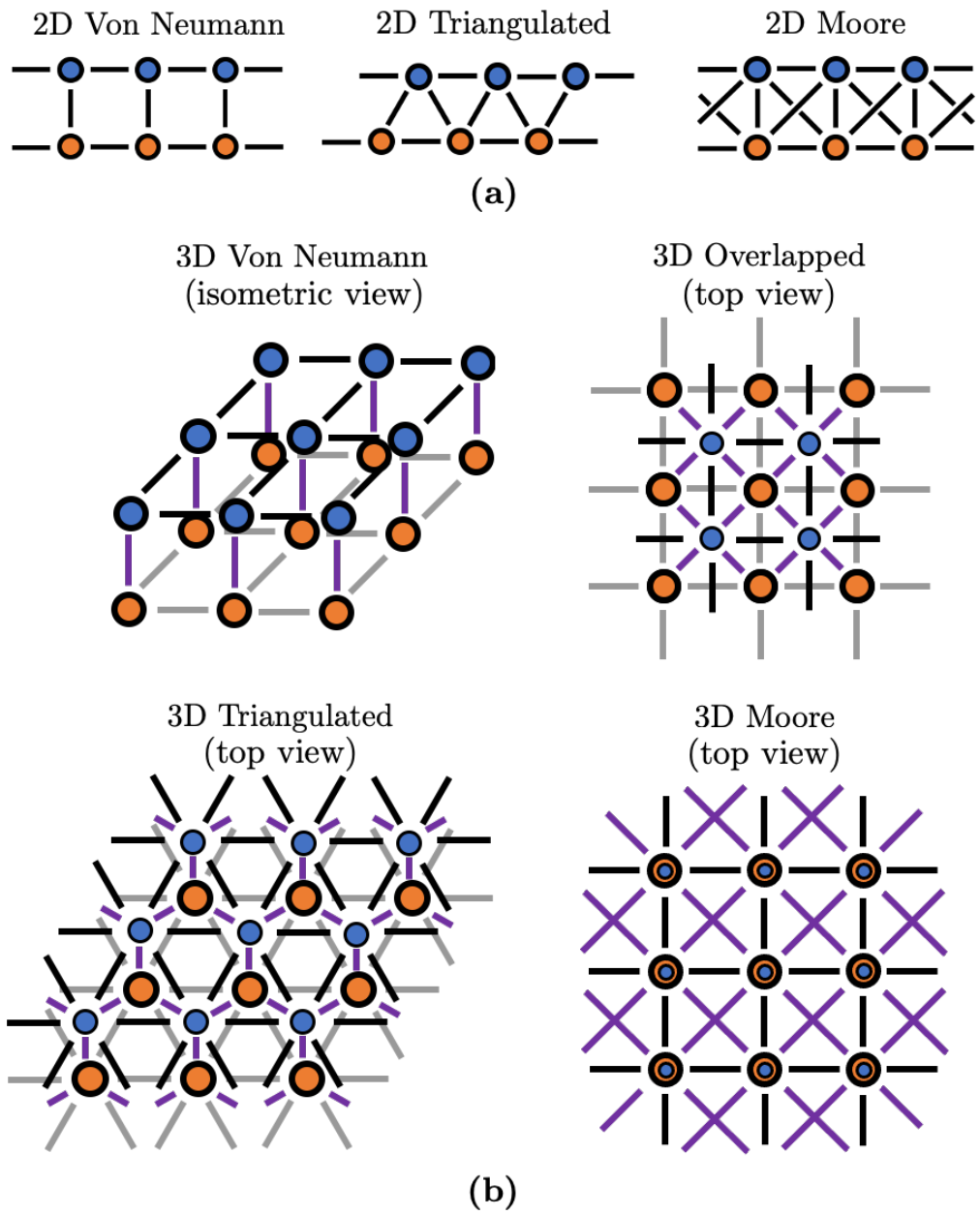

FIGURE 5. Connectivity diagrams of the bilayer mammary organoid. Basal cells are shaded blue and luminal cells are shaded orange. (a) Representative diagrams of 2D geometries studied, solid black lines correspond to cellular connections. (b) Schematics of 3D lattices, grey lines correspond to connections between luminal cells, black lines are connections between basal cells and purple lines represent connections between the layers.

In this section, we recast the classical NDM (2.1-2.2) into an interconnected dynamical system using cell-type dependent weighted graphs and outlined the specific edge structures we consider in our computations. This enables the analysis of cellular connectivity structure coupled to the intracellular kinetics in large-scale systems, providing a general approach to intercellular interactions. In the following section, we discuss

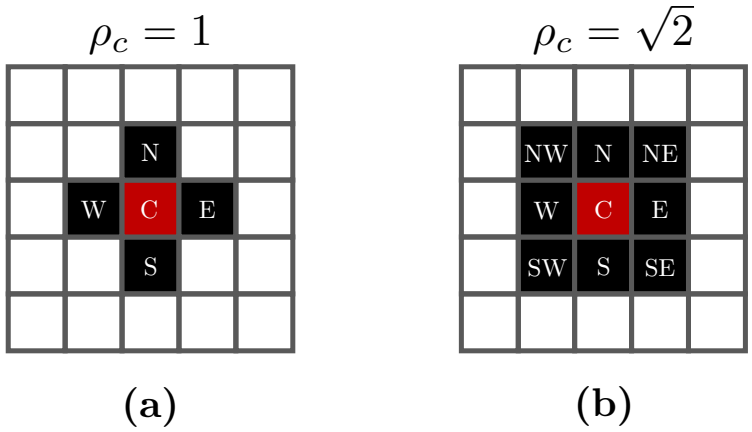

FIGURE 6. A diagram of the cellular neighbourhoods defined by (a) Von Neumann and (b) Moore on an unitary static grid lattice.

methods of reducing the size of the large-scale systems, while preserving the connectivity structure of the graphs.

2.3. **Graph partitioning for large-scale system dimension reduction.**

This study applies the pattern analysis framework of Ferreira et al. (2013) to edge weight anisotropic bilayer graphs. Specifically, in [18] the symmetries of the cellular connectivity graph $\mathcal{G} = \mathcal{G}(V, E)$ were used to develop analytical conditions for the existence and stability of inhomogeneous steady states in lateral-inhibition ODE models independent of the precise tissue geometry. These methods were employed by considering contrasting pattern states of cells as partitions of the graph which can be viewed as a pre-defined pattern template. A graph partition π is the grouping of vertices $v \in V$ into the sets $P_i \subseteq V$ such that the subsets P_i are disjoint [28]. For example, each cell in $\mathcal{G}$, represented by a vertex $v \in V$, can be collected into a set that converges to the same biochemical state, thus producing subsets of V defining the graph partition π (Figure 7a). Using graph partitions, we define two additional properties that are key for the analysis conducted in [17, 18] for pattern analysis in large-scale interconnected systems.

Equitable partitions are those that preserve the underlying structure of a graph $\mathcal{G}$ by using the regularity (symmetries) of the edge structure such that all vertices $v_j \in P_i$ have the same number of edges with identical weights. Thereby selecting representative cells from each subset P_i we generate a quotient graph that has the potential to reduce the number of vertices in the graph whilst retaining the topology of the original connectivity. Figure 7a illustrates the reduction of a cell-type stratified bilayer regular graph to a quotient graph of only two representative vertices.

Definition 2.1 (Equitable partitions and quotient graphs [29])**.** *Let $\mathcal{G} = \mathcal{G}(V, E)$ be a graph with adjacency matrix $\boldsymbol{W}$. Consider a partition of π of $\mathcal{G}$ that allocates each vertex $v \in V$ into one of the sets $P_1, ..., P_k$.*

The partition π is said to be equitable if there exists $\overline{w}_{ij}$ for all $i, j \in \{1, ..., k\}$ such that

$$\sum_{v \in P_j} w_{uv} = \overline{w}_{ij} \quad \forall u \in P_i, \tag{2.9}$$

where w_{ij} are the elements of $\boldsymbol{W}$. Moreover, the graph of a single representative vertex from each partition $P_1, ..., P_k$ constructed from the reduced adjacency matrix $[\overline{w}_{ij}] = \overline{\boldsymbol{W}}$ is called the quotient graph and is denoted by $\mathcal{G}/\pi = \mathcal{G}_\pi$.

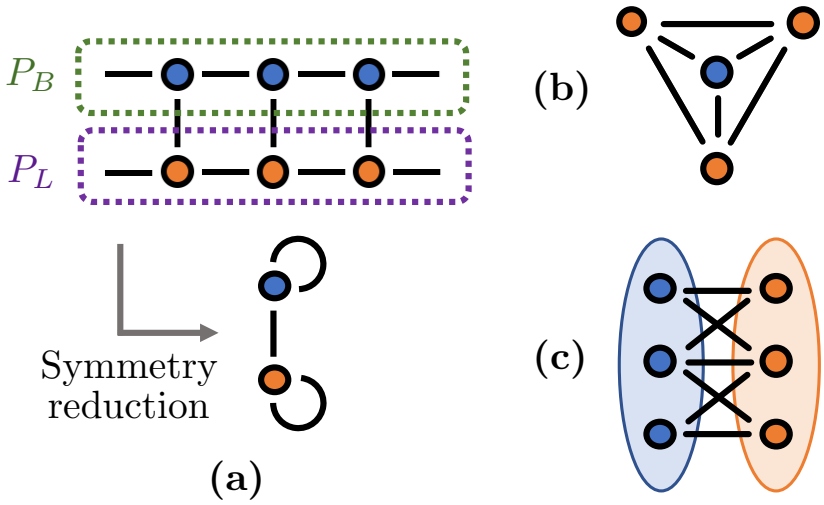

FIGURE 7. Graph partitioning, symmetry reduction and example graphs. (a) A diagram representing the partitioning and symmetry reduction process for a bilayer structure of two subpopulations representing a mammary organoid, see Section 2.2. The graph defining the bilayer is partitioned into layers, such that basal cells lie in the partition P_B and luminal cells lie in the partition P_L. By exploiting the symmetries of edge connectivity, a reduction of vertices is made to consider only representative cells from each partition, P_B and P_L, generating a quotient graph. (b) An example graph with the equitable partitions property. The partitions are highlighted using colours, the diagram highlights that the blue node always has three connected orange nodes, and any orange node has only one blue node connected. (c) An example graph with the bipartite property. The full graph consisting of both blue and orange nodes can be decomposed into two disjoint sets of vertices highlighted by the shaded regions.

Intuitively if π is an equitable partition of $\mathcal{G}$, then the edge structure, namely, the number of edges and associated edge weights are identical independent of the choice of vertices in the same set P_i. An example of an equitable partition π with two vertex sets P_1 and P_2 is given in Figure 7b. Furthermore, we introduce an additional graph property that is required for monotone system transformations that are discussed in the following section.

Definition 2.2 (Bipartite graphs [28])**.** *A graph $\mathcal{G}$ is said to be bipartite if $\mathcal{G}$ can be constructed by the union of two disjoint sets of vertices such that no vertices within the same set are connected.*

Figure 7c depicts an example of a bipartite graph. The bipartite property of a graph $\mathcal{G}$ need not induce the regular structure as is the case of an equitable partition however it can limit the types of connectivity possible, which may detract from the biological relevance of the connectivity graphs in large-scale systems as discussed in [17]. Although, it has been shown that the bipartite property of the quotient graph is not a restriction in the case of two distinct subpopulations [18].

To apply the results of [18] to the bilayer tissue geometries that we consider in this study, we make the following assumptions on the connectivity graphs:

(A1) There exists an equitable partition π_2 of the graph $\mathcal{G}$ that groups the vertices into two sets P_1 and P_2;

(A2) The quotient graph $\mathcal{G}_{\pi_2}$ is bipartite omitting self-loops.

The 2D and 3D bilayer structures outlined in Section 2.2 conform to (A1) and (A2) as we assume each layer of the N_c-regular graph is constructed from cells of the same type, for example see Figures 5 and 7a. Critically, Ferreira et al. (2013) use (A1) and (A2) to develop methods of pattern templating, namely, using quotient graphs to generate a pre-defined pattern structure for contrasting states of representative cells [18]. Specifically, the dimension reduction from the equitable partition π acts on the scaled weighted adjacency matrix $\boldsymbol{W}_0 = (1/N_w)\boldsymbol{W}$ as constructed in Section 2.2 such that for two representative cells in the bilayer system, the scaled reduced adjacency matrix has the form

$$\overline{\boldsymbol{W}}_0 = \begin{bmatrix} \frac{n_1 w_1}{n_1 w_1 + n_2 w_2} & \frac{n_2 w_2}{n_1 w_1 + n_2 w_2} \\ \frac{n_2 w_2}{n_1 w_1 + n_2 w_2} & \frac{n_1 w_1}{n_1 w_1 + n_2 w_2} \end{bmatrix}, \tag{2.10}$$

following from the connectivity symmetry of $\mathcal{G}$ induced from the regular edge structure.

Informally, the reduced scaled adjacency matrix (2.10) represents the connectivity of the partitions as proportional values between representative cells from each partition, where we consider each partition to contain a single cell type (Figure 7a). Substituting the quotient graph for cellular connectivity into the interconnected dynamical system constructed in sections 2.1 and 2.2 generates a quotient dynamical system which is more amenable to deriving analytic bounds on signal polarity for laminar pattern formation.

We have shown that the large-scale interconnected ODE systems can be reduced to smaller, analytically tractable quotient systems for bilayer regular structures of two distinct subpopulations. In the following section, we further discuss interconnected systems in generality and existing results that leverage properties of the intracellular kinetics and their associated connectivity graphs to isolate the spatial and temporal influence on pattern convergence.

2.4. **Monotone interconnected dynamical systems.**

The interconnected lateral-inhibition model constructed in sections 2.1 and 2.2 can be generalised to form single-input-single-output system (SISO), a common representation of interconnected ODEs in control theory with a single state variable connecting the respective subsystems [30]. Formally, the SISO of a lateral feedback model has the form, for each cell $i \in \{1, ..., \mathcal{N}\}$,

$$\dot{\boldsymbol{x}}_i = \boldsymbol{f}\left(\boldsymbol{x}_i, u_i\right), \tag{2.11}$$

$$y_i = h\left(\boldsymbol{x}_i\right), \tag{2.12}$$

where $\boldsymbol{x}_i \in X$ is a vector of reactants (e.g. Notch and Delta), $u_i \in U$ is the input value to each cell, determined by the discrete spatial operator $\langle\cdot\rangle$ and $y_i \in Y$ is the output of cell i to its connected neighbours. Namely, for $\boldsymbol{u} = [u_1, ..., u_{\mathcal{N}}]^T$ and $\boldsymbol{y} = [y_1, ..., y_{\mathcal{N}}]^T$, we have that $\boldsymbol{u} = \boldsymbol{W}_0\boldsymbol{y}$. The function $\boldsymbol{f} : X \times U \to X$ defines the nonlinear dynamics of the feedback model, and $h : X \to Y$ is the function defining the relationship between the intracellular kinetics and the output signals of the cell. It is assumed that both $\boldsymbol{f}$ and h are continuously differentiable. A diagram of cell-cell lateral-inhibition interactions from the perspective of a SISO system are given in Figure 8.

For example, for the lateral-inhibition model defined by the NDM (2.1-2.2), we have that $\boldsymbol{x}_i = [N_i, D_i]^T$, where the internal kinetics are of the form,

$$\boldsymbol{f}\left([N_i, D_i]^T, u_i\right) = \begin{bmatrix} f\left(u_i\right) - \mu_1 N_i \\ g\left(N_i\right) - \mu_2 D_i, \end{bmatrix} \tag{2.13}$$

for $f\left(\cdot\right)$ and $g\left(\cdot\right)$ the increasing and decreasing functions as defined in Section 2.1. The output signal of each cell is the current Delta value $y_i = h\left([N_i, D_i]^T\right) = D_i$, and thus the input signal of cell i is determined by the connectivity structure of $\mathcal{G}$ such that $u_i = \left(\boldsymbol{W}_0\boldsymbol{D}\right)_i$. As we consider the input signals u_i to be composed of only a linear combination of output signals y_j from other cells, the interconnected system defined by the NDM (2.1-2.2) is closed-loop with no external stimuli.

In order to summarise the internal dynamics of each cell, we introduce the characteristic transfer function $T : U \to Y$, which defines the input to output signal transfer of the dynamical system for each cell,

$$T(\cdot) := h\left(S(\cdot)\right), \tag{2.14}$$

where $\boldsymbol{S} : U \to X$ maps the information from connected cells to the intracellular dynamical system (2.11). Namely, the function $\boldsymbol{S}\left(\cdot\right)$ is the solution to the intracellular dynamical system (2.11) for input signal $u \in U$. As we consider the transfer function to emulate the cellular response to receptor activation, it is assumed that

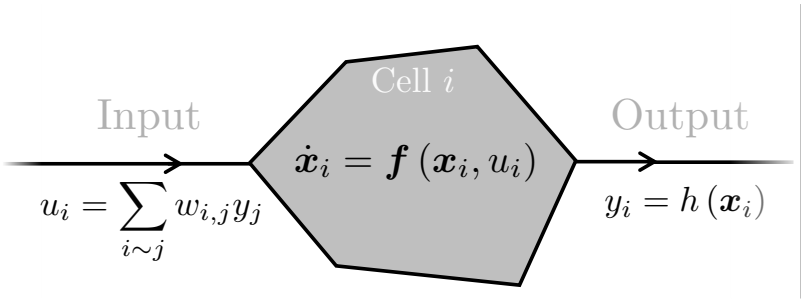

FIGURE 8. A signal flow diagram for a single cell in a SISO interconnected lateral-inhibition system. The scalar input signal u_i is the determined by the output signals of the connected cells to cell i via the connectivity graph $\mathcal{G}$, namely, $i \sim j$ if cell i and cell j are in contact, where each output signal strength y_j is mediated by the edge weight $w_{i,j}$. The input signal u_i then stimulates a response from cell i which is determined by the intracellular dynamical system $\dot{\boldsymbol{x}}_i = \boldsymbol{f}(\boldsymbol{x}, u_i)$. The resultant changes to the state variables $\boldsymbol{x}_i$ update the output signals of the cell y_i thereby influencing the behaviour of those cells connected to cell i.

$T(u_i)$ is positive and bounded, and characteristically, $T(u_i)$ is a decreasing function for lateral-inhibition and increasing for lateral-induction [17]. For the nonlinear dynamics required to produce patterning via lateral-inhibition mechanisms [31], the characteristic transfer function, $T(u_i)$, is generally algebraically intractable as it is constructed by the composition of nonlinear functions that define the intracellular kinetics [17].

Although directly intractable, we can use the standard method of linearisation to gain insights into the behaviour of the transfer function (2.14). We do not present the derivation here (see [17] for details) but it can be shown that the derivative of the transfer function (2.14) can be linearly approximated by

$$T'(u) = -\left(\frac{\partial h}{\partial \boldsymbol{x}}\right)\left(\frac{\partial \boldsymbol{f}}{\partial \boldsymbol{x}}\right)^{-1}\left(\frac{\partial \boldsymbol{f}}{\partial u}\right)\Bigg|_{\boldsymbol{x}=\boldsymbol{S}(u)} = -\boldsymbol{C}\boldsymbol{A}^{-1}\boldsymbol{B}. \tag{2.15}$$

Namely, the components $\boldsymbol{A}$, $\boldsymbol{B}$ and $\boldsymbol{C}$ form the linearised SISO system

$$\dot{\boldsymbol{x}}_i = \boldsymbol{A}\boldsymbol{x}_i + \boldsymbol{B}u_i, \tag{2.16}$$

$$y_i = \boldsymbol{C}\boldsymbol{x}_i, \tag{2.17}$$

near points of interest in the input, output and internal spaces U, Y and $\boldsymbol{X}$ respectively such that the linearised components are evaluated with respect to a given input u_s by

$$\boldsymbol{A} = \left(\frac{\partial \boldsymbol{f}}{\partial \boldsymbol{x}}\right)\Bigg|_{\boldsymbol{x}=\boldsymbol{S}(u_s)} \quad \boldsymbol{B} = \left(\frac{\partial \boldsymbol{f}}{\partial u}\right)\Bigg|_{\boldsymbol{x}=\boldsymbol{S}(u_s)} \quad \boldsymbol{C} = \left(\frac{\partial h}{\partial \boldsymbol{x}}\right)\Bigg|_{\boldsymbol{x}=\boldsymbol{S}(u_s)}. \tag{2.18}$$

A key property of SISO lateral-inhibition models is monotonicity of the transfer function $T(u_i)$. Monotone interconnected systems preserve the order of trajectories within respective nonempty subsets of *Banach* spaces [32]. Namely, if $\boldsymbol{\phi}(\boldsymbol{x}^*, t) = \boldsymbol{\phi}_t(\boldsymbol{x}^*)$, is the solution to a monotone dynamical system for initial condition $\boldsymbol{x}^*$, then $\boldsymbol{\phi}_t(\boldsymbol{x}_1) \leq \boldsymbol{\phi}_t(\boldsymbol{x}_2)$ for all $\boldsymbol{x}_1 \leq \boldsymbol{x}_2$ and $t \in (0, \infty]$. However to formerly define such ordering of solutions

for interconnected systems, we first need to introduce the spaces that the input, output and internal kinetics lie in, known as trajectory spaces.

The trajectory spaces, $K \subset \mathbb{R}^n$, we consider are generalisations of orthants in Euclidean space and have the following properties:

(1) K is a cone, that is, $\alpha k \in K$ for all $\alpha \in \mathbb{R}_{\geq 0}$ and $k \in K$.

(2) K is convex, for any $\alpha, \beta \in \mathbb{R}_{\geq 0}$ and $k_1, k_2 \in K$ then $\alpha k_1 + \beta k_2 \in K$.

(3) K is pointed, namely, $\{0\} \in K$.

An example the above properties of the trajectory space is shown in Figure 9. The systems we consider represent intracellular protein activation an thus always lie in the positive orthant (i.e. $\boldsymbol{x}_i, u_i, y_i \geq 0$) which conforms to the properties of the pointed, convex cone, K. However, the positivity of these cones may alter following a coordinate transformation thus requiring the general definition stated above. Given a cone K, we define partial ordering of elements via "$\preceq$" such that for $\boldsymbol{x}, \hat{\boldsymbol{x}} \in K$, then $\boldsymbol{x} \preceq \hat{\boldsymbol{x}}$ means that $\hat{\boldsymbol{x}} - \boldsymbol{x} \in K$ [17]. The trajectory spaces of the interconnected system (2.11-2.12) $\boldsymbol{X}, U$ and Y, can be defined as cones $K^{\boldsymbol{X}}, K^U$ and K^Y as they are closed and bounded vector spaces of $\mathbb{R}^n$ [32]. The monotonicity of SISO systems (2.11-2.12) is defined as follows.

Definition 2.3 (Monotone SISO interconnected systems [32])**.** *Given the cones $K^U, K^Y, K^{\boldsymbol{X}}$ for the input, output and state spaces, respectively, the input-output ODE model $\dot{\boldsymbol{x}}_i = \boldsymbol{f}(\boldsymbol{x}, u_i)$, $y_i = h(\boldsymbol{x}_i)$ is said to be monotone if $\boldsymbol{x}_i(0) \preceq \hat{\boldsymbol{x}}_i(0)$ and $u_i(t) \preceq \hat{u}_i(t)$ for all $t \geq 0$ imply that the resulting solutions satisfy $\boldsymbol{x}_i(t) \preceq \hat{\boldsymbol{x}}_i(t)$ for all $t \geq 0$, and the output map is such that $\boldsymbol{x}_i \preceq \hat{\boldsymbol{x}}_i$ implies $h(\boldsymbol{x}_i) \preceq h(\hat{\boldsymbol{x}}_i)$.*

It has previously been shown that the interconnected system defined by the NDM (2.1-2.2) is monotone with respect to the cones $K^U = \mathbb{R}_{\geq 0}$, $K^Y = \mathbb{R}_{\leq 0}$ and $K^{\boldsymbol{X}} = \{\boldsymbol{x} \in \mathbb{R}^2 : x_1 \geq 0, x_2 \leq 0\}$ [17]. These cones outline the characteristic behaviour of the lateral-inhibition mechanism such that if the input signals of Delta from adjacent cells are monotonically increasing, we expect the output signal of Delta in the central cell to be monotonically decreasing.

The monotonicity of SISO systems (2.11-2.12) have previously been used to investigate the stability of component-wise steady states in biological contexts [17, 18, 32]. Namely, monotone interconnected systems yield predictable behaviour via the trajectory cones and thus the geometry of the cellular domain can be manipulated using the connectivity graph $\mathcal{G}$ to achieve the desired states for the cells.

In control theory, the stability of SISO systems (2.11-2.12) can be assessed by analysing the transition of inputs and output between components of the connected system. A particular measure of a connected system is the $\mathcal{L}_2$-gain, which is a nonnegative quantity that describes the response of a system to an input. We first provide a general definition of a $\mathcal{L}_p$-gain.

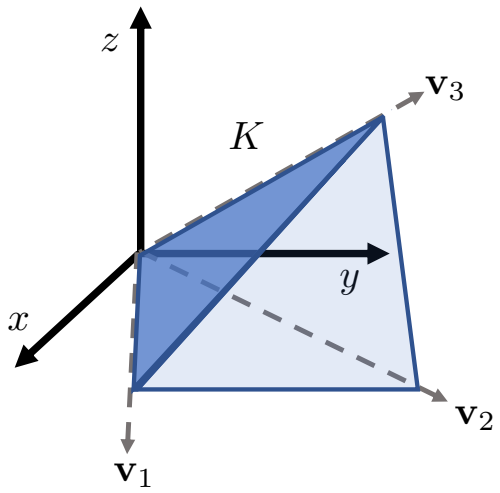

FIGURE 9. An example of a pointed, convex cone K in Euclidean space, where $K = \{\boldsymbol{x} \in \mathbb{R}^3 : \boldsymbol{x} = a_1\mathbf{v}_1 + a_2\mathbf{v}_2 + a_3\mathbf{v}_3 \ \forall a_i \in \mathbb{R}_{\geq 0}\}$.

Definition 2.4 ($\mathcal{L}_p$-gain of a SISO system [33])**.** *The $\mathcal{L}_p$-gain, $q_{i,p} > 0$, of a SISO system (2.11-2.12) is defined by*

$$q_{i,p} = \sup_{t \leq \tilde{t}} \left(\frac{||y_i(t)||_p}{||u_i(t)||_p} \right) \tag{2.19}$$

for all y_i and $u_i \neq 0$ for $i = 1, ..., N$, and $\tilde{t} > 0$ denotes the truncation of the Hilbert spaces for the input and outputs of the system, $\mathcal{L}_p(U)$ and $\mathcal{L}_p(Y)$, respectively.

The $\mathcal{L}_p$-gain, $q_{i,p}$, is the maximal ratio of output to input over a specified region of time for the output and input domains defined generally by Hilbert spaces. In the biological systems we consider, all functions are smooth, continuous and differentiable and thus satisfy these general conditions. However, the $\mathcal{L}_p$-gains of a interconnected system require analytic forms of inputs, $u_i(t)$, and outputs, $y_i(t)$ for each cell which are not obtainable in large-scale nonlinear systems. Although, for monotone systems such that the output map $h(\boldsymbol{x}) \geq 0$ for all $\boldsymbol{x} \in X$, we have that the $\mathcal{L}_2$-gains of a nonlinear SISO system can be approximated by

$$q_{i,2} = |-\boldsymbol{C}\boldsymbol{A}^{-1}\boldsymbol{B}| = |T'(u_i^*)| \tag{2.20}$$

for the linearisation of the SISO system about the steady input state, u_i^*, as derived previously (see [34] for derivation). Critically, the output signals we consider in the biological systems represent protein activation and thus are nonnegative, i.e. we have that $h(\boldsymbol{x}) \geq 0$ for all $\boldsymbol{x} \in X$ is always satisfied. Therefore, by demonstrating a nonlinear SISO system is monotone, we have a convenient procedure to compute the $\mathcal{L}_2$-gains for each cell in order to measure the output signal response to input perturbations, providing a control measure of cell state stability. For the remainder of the study, we consider only the $\mathcal{L}_2$-gains for each cell as this is the standard norm for the Euclidean vector spaces, therefore we set $q_{i,2} = q_i$.

The $\mathcal{L}_2$-gains of interconnected SISO systems are particularly useful for understanding the stability of the feedback between the connected components. The Small Gain theorem yields a sufficient bound on two interconnected components for the global stability of feedback.

Theorem 2.1 (Small Gain theorem [33])**.** *For all bounded inputs, a SISO system (2.11-2.12) of two interconnected cells c_1 and c_2, in a closed-loop are locally asymptotically stable if c_1 and c_2 are independently stable and*

$$q_1 q_2 < 1, \tag{2.21}$$

where q_1 and q_2 are the $\mathcal{L}_2$-gains of c_1 and c_2, respectively.

In terms of multicellular systems we consider, Theorem 2.1 states that given that intracellular kinetics are not self-exciting in isolation, i.e. $\boldsymbol{A}$ is stable, then the interconnection of these two cells remain globally stable provided their respective gains (transfer function dynamics, $T'(u_i)$) are suitably bounded. The application of an equitable partition π to generate a quotient graph $\mathcal{G}_\pi$ consisting of only two representative cells allows for the use of Theorem (2.1) in the quotient interconnected systems representing cell-type stratified bilayer geometries that we consider in this study.

We now present the results previously derived in [18] that generate and maintain binary patterns in large-scale interconnected SISO systems using the monotonicity of the lateral-inhibition mechanisms and regularity of the cellular connectivity structures via equitable partitions. The first result we consider provides a simple condition for the instability of the homogeneous steady state of the quotient interconnected SISO system. Critically, provided the SISO system (2.11-2.12) is monotone with a bounded transfer function, the instability of the homogeneous steady state yields the convergence to contrasting fixed states for each representative cell.

Theorem 2.2 ([18])**.** *Let π be an equitable partition of $\mathcal{G}$ such that (A2) is satisfied. Let $\overline{\lambda}_r$ the smallest eigenvalue of reduced quotient matrix associated with $\mathcal{G}_\pi$. If the output characteristic function, $T(u_i)$, is positive, bounded and decreasing, and if for the homogeneous input steady state, u^*, we have*

$$|T'(u^*)|\overline{\lambda}_r < -1, \tag{2.22}$$

then there exists heterogeneous steady states in the representative vertices of $\mathcal{G}_\pi$.

The second result derived in [18] that we consider defines conditions for the stability of heterogeneous steady states via $\mathcal{L}_2$-gains of the representative cells within the quotient system. By exploiting the regularity of the large-scale connectivity graph, and therefore assuming each cell within the same partition behaves identically, the $\mathcal{L}_2$-gains for those cells will also be identical. Let $\overline{\boldsymbol{Q}} = \mathrm{diag}\{q_1, ..., q_k\}$ represent the $\mathcal{L}_2$-gains

from each representative cell in each patterning partition $P_1, ..., P_k$. In addition, if $\boldsymbol{A}$ is a square matrix with the set of eigenvalues $\sigma(\boldsymbol{A})$, then the spectral radius of $\boldsymbol{A}$ is defined by

$$\rho(\boldsymbol{A}) = \max\{|\lambda| : \lambda \in \sigma(\boldsymbol{A})\}. \tag{2.23}$$

Using the spectral properties of the connected graph defined by the cellular domain, the stability criterion for the heterogeneous steady states is stated as follows.

Theorem 2.3 ([18])**.** *Consider the quotient system as defined in Theorem 2.2. The steady state pattern defined by heterogeneous steady states are locally asymptotically stable if*

$$\rho\left(\overline{\boldsymbol{M}}\,\overline{\boldsymbol{Q}}\right) < 1, \tag{2.24}$$

where $\overline{\boldsymbol{M}}$ is a reduced quotient adjacency matrix that satisfies (A1) and (A2), and $\rho(\cdot)$ represents the spectral radius.

The application of Theorem 2.2 and Theorem 2.3 to the signal anisotropic bilayer geometries defined in sections 2.2 and 2.3 allow us to derive conditions for the amount of signal polarisation for a given connectivity structure that required to generate and maintain laminar patterns using lateral-inhibition kinetics.

3. Existence and stability of laminar pattern formation in quotient SISO systems

In this section we derive conditions on the cell-type signal weights w_1 and w_2 of the connectivity graphs constructed in sections 2.2 and 2.3 that yield the existence and stability of heterogeneous states in quotient bilayer systems. Specifically, by leveraging the monotone properties of the quotient SISO systems, we significantly reduce the complexity involved in juxtacrine pattern analysis in multicellular systems to investigate the role of anisotropic cellular connectivity in cell state stratification.

3.1. **Conditions on cell-type signal strength for the existence of bilayer laminar patterns.**

We apply Theorem 2.2 to the reduced geometry of a bilayer periodic lattice described in Section 2.3. The following result yields a distinct monotonic relationship between homotypic and heterotypic signal weights when we consider the vertex sets P_1 and P_2 of $\mathcal{G}$ to contain basal and luminal cells, respectively, as shown in Figure 7a.

Theorem 3.1. *Let $\mathcal{G}$ be an undirected, connected graph that satisfies (A1) and (A2) where the quotient graph $\mathcal{G}_\pi$ has the associated reduced scaled adjacency matrix as defined in (2.10). Consider $T(\cdot)$ the transfer function of a lateral-inhibition SISO system (2.11-2.12) such that $T(\cdot)$ is positive, bounded and decreasing.*

Then there exists heterogeneous steady states between partitions P_1 and P_2 if

$$w_1 < \left(\frac{|T'(u^*)| - 1}{|T'(u^*)| + 1} \right) \frac{w_2}{R_\tau}, \tag{3.1}$$

provided that $n_1 w_1 < n_2 w_2$.

Proof. The result follows directly from the application Theorem 2.2 to the regular bilayer structures with layer stratified cells-types that define the sets P_1 and P_2. Specifically, we consider the general quotient reduced matrix $\overline{\boldsymbol{W}}_0$ as defined in (2.10) and seek the smallest eigenvalue. By directed computation we have that

$$\sigma\left(\overline{\boldsymbol{W}}_0\right) = \left\{ \lambda_1 = 1, \lambda_2 = \frac{n_1 w_1 - n_2 w_2}{n_1 w_1 + n_2 w_2} \right\}. \tag{3.2}$$

As $\lambda_2 < \lambda_1$ independent of the bilayer geometry, and, we have $\lambda_2 < 0$ from the assumption that $n_1 w_1 < n_2 w_2$ then $\lambda_2 = \overline{\lambda}_r$ in Theorem 2.2. Applying Theorem 2.2 to the bilayer geometry, we substitute λ_2 into inequality (2.22) as follows

$$|T'(u^*)| \left(\frac{n_1 w_1 - n_2 w_2}{n_1 w_1 + n_2 w_2} \right) < -1, \tag{3.3}$$

which can be rearranged to yield inequality (3.1). □

Inequality (3.1) bounds the cell-type dependent signal strength and highlights the influence of cellular connectivity on pattern formation via the R_τ. For example, as we increase the number of connected cells within the same partition (n_1) then we require greater amounts of signal polarisation (edge weight anisotropy) directed towards those cells within the other partition to induce laminar patterns, i.e. w_1 must decrease.

3.2. **Conditions on cell-type signal strength for the stability of bilayer laminar patterns.**

By applying Theorem 2.3 to the geometry of the general quotient representation of the bilayer of cells (2.10) yields the following restriction on the homotypic and heterotypic signal strength parameters, w_1 and w_2, for the stability of the heterogeneous states that are produced by Theorem 3.1. Namely, the following statement provides sufficient signal polarisation conditions for the maintenance of laminar pattern formation between static cells in each partition P_1 and P_2.

Theorem 3.2. *Let $\mathcal{G}$ be an undirected, connected graph that satisfies (A1) and (A2) where the quotient graph $\mathcal{G}_\pi$ has the associated reduced scaled adjacency matrix as defined in (2.10). Consider the $\mathcal{L}_2$-gains of the representative cells, q_1 and q_2 from the partitions P_1 and P_2 associated with the heterogeneous steady states $\boldsymbol{x}_1$ and $\boldsymbol{x}_2$, respectively. Then if any of the following gain relations hold:*

(i) $q_1 + q_2 \leq 2$

(ii) $q_1 + q_2 > 2 \quad \textit{and} \quad w_1 < \left(\frac{2}{q_1+q_2-2}\right)\frac{w_2}{R_\tau}$

then the local asymptotic stability of the heterogeneous steady states $\boldsymbol{x}_1$ *and* $\boldsymbol{x}_2$ *is guaranteed if*

$$\frac{n_1 w_1}{n_1 w_1 + n_2 w_2}\left(q_1 + q_2 - 2q_1 q_2\right) < 1 - q_1 q_2 \tag{3.4}$$

is satisfied. Moreover if $q_1 > 1$ *and* $q_2 < 1$*, or vice versa, then the laminar pattern stability criterion (3.4) has the form*

$$w_1 < \left(\frac{1 - q_1 q_2}{q_1 + q_2 - q_1 q_2 - 1}\right)\frac{w_2}{R_\tau}. \tag{3.5}$$

Proof. Consider the reduced scaled weighted adjacency matrix $\overline{\boldsymbol{W}}_0$ (2.10) associated with the cell-type partitioned quotient graph $\mathcal{G}_\pi$. Let $a = n_1 w_1 / N_w$ and $b = n_2 w_2 / N_w$ and therefore we have,

$$\overline{\boldsymbol{W}}_0\,\overline{\boldsymbol{Q}} = \begin{bmatrix} aq_1 & (1-a)q_2 \\ (1-a)q_1 & aq_2 \end{bmatrix}, \tag{3.6}$$

where $b = (1-a)$ due to the row stochastic property of the reduced adjacency matrix $\overline{\boldsymbol{W}}_0$. The matrix $\overline{\boldsymbol{W}}_0\,\overline{\boldsymbol{Q}}$ is nonnegative as each entry is product of nonnegative values. By the Perron–Frobenius theorem [35], $\rho\left(\overline{\boldsymbol{W}}_0\,\overline{\boldsymbol{Q}}\right)$ is an eigenvalue of $\overline{\boldsymbol{W}}_0\,\overline{\boldsymbol{Q}}$, which is real due to the positivity of the matrix. Solving for the eigenvalues of $\overline{\boldsymbol{W}}_0\,\overline{\boldsymbol{Q}}$ yields

$$\rho\left(\overline{\boldsymbol{W}}_0\,\overline{\boldsymbol{Q}}\right) = \frac{a\left(q_1+q_2\right)}{2} + \frac{\sqrt{a^2\left(q_1-q_2\right)^2 + 4\left(1-a\right)^2 q_1 q_2}}{2}, \tag{3.7}$$

and so by applying Theorem 2.3 to the spectral radius (3.7), we ensure for the local asymptotic stability of the heterogeneous states associated with q_1 and q_2. If the necessary conditions (i) or (ii) for pattern stability are satisfied, then we have that

$$\sqrt{a^2\left(q_1-q_2\right)^2 + 4(1-a)^2 q_1 q_2} < 2 - a\left(q_1+q_2\right) \tag{3.8}$$

is well-defined as the left most term of inequality (3.8) must be real and positive by the Perron–Frobenius theorem. Namely, Theorem 2.3 can only be satisfied provided the conditions (i) or (ii) hold. Subsequently, both sides of inequality (3.8) are positive and therefore squaring both sides perseveres the inequality, which can be expanded and rearranged as follows

$$q_1 q_2\left((1-a)^2 - a^2\right) + a\left(q_1+q_2\right) < 1 \tag{3.9}$$

which yields inequality (3.4) from further rearrangement.

In the case where $q_1 > 1$ and $q_2 < 1$ (or $q_1 < 1$ and $q_2 > 1$), then $(q_1 - 1)(q_2 - 1) < 0$. Moreover, this implies that

$$q_1 + q_2 > 1 + q_1 q_2. \tag{3.10}$$

after expansion. In addition, inequality (3.9) can be arranged to following form

$$n_1 w_1 (q_1 + q_2 - q_1 q_2 - 1) < (1 - q_1 q_2) n_2 w_2. \tag{3.11}$$

Therefore by inequality (3.10) the left most terms of inequality (3.11) are positive and so division of inequality (3.11) by $(q_1 + q_2 - q_1 q_2 - 1)$ preserves direction of the inequality, producing the pattern stability criterion explicitly in terms of signal weights w_1 and w_2. □

Corollary 3.1. *If the homogeneous steady state u^* of a monotone SISO system (2.11-2.12) yields $|T'(u^*)| \geq 3$, then the gain relation (ii) in Theorem 3.2 is always satisfied.*

Proof. Without loss of generality, we have that $q_2 < |T'(u^*)| < q_1$ as the contrasting input states u_1 and u_2 will diverge from u^* in opposing directions by the monotonicity of the SISO reduced system [18]. From inequality (3.1) we know that $1 < q_1$ must hold as $w_1 \in \mathbb{R}_{\geq 0}$, that is $|T'(u^*)| > 1$ is required for the existence of laminar patterns. Therefore, if we assume that the homogeneous steady state of the monotone SISO system (2.11-2.12) is unstable, producing contrasting states in the representative cells, then inequality (3.1) is satisfied. Comparing the pattern existence inequality (3.1) and the necessary condition (ii) for pattern stability, we have that inequalityitem (ii) holds when

$$\frac{1}{q_1 - 1} < \frac{2}{q_1 + q_2 - 2} < \frac{|T'(u^*)| - 1}{|T'(u^*)| + 1}, \tag{3.12}$$

where the left-most term follows from $q_2 < q_1$. Rearranging inequality (3.12) yields

$$\frac{2|T'(u^*)|}{|T'(u^*)| - 1} < q_1, \tag{3.13}$$

then applying our assumption $|T'(u^*)| < q_1$, inequality (3.13) can be satified by solving the more restrictive bound

$$\frac{2|T'(u^*)|}{|T'(u^*)| - 1} < |T'(u^*)|, \tag{3.14}$$

which has the minimum value of $|T'(u^*)| = 3$. Moreover, this implies that $q_1 > 3$ which immediately satisfies $q_1 + q_2 > 2$, and therefore condition (ii) holds. □

Inequality (3.4) outlines the relationship between cellular connectivity (n_1, n_2) and signal protein feedback (w_1, w_2) that is required to be balanced to ensure the maintenance of pattern formation in bilayer static geometries. However, we note that the $\mathcal{L}_2$-gains are dependent on the geometry, as they are a function

of the input value defined by the discrete spatial operator $\langle\cdot\rangle$, see Definition 2.4. Thus, inequality (3.4) cannot determine explicit conditions for the relationship between geometry and feedback model, as in the existence inequality (3.1). However, provided the $\mathcal{L}_2$-gains of the representative cells satifsfy the appropriated conditions outlined in Theorem 3.2, inequalities (3.1) and (3.5) are in a directly comparable form with respect to signal transfer dynamics.

In addition, inequality (3.9) and therefore inequality (3.5) describes a relaxation of the Small Gain theorem for closed-loop system, commonly used in control theory applications [36]. To demonstrate this relaxation of the Small Gain a theorem, w.l.o.g. assume that $q_2 < q_1$, as we expect the partitions P_1 and P_2 of $\mathcal{G}$ to obtain contrasting solution states. In this case, inequality (3.9) is bounded from above by setting $q_2 = q_1$,

$$q_1 q_2 \left(1 - 2a\right) + a\left(q_1 + q_2\right) < q_1 \left(\left(1 - 2a\right) q_1 + 2a\right), \tag{3.15}$$

where $a = n_1 w_1 / N_w$ as in Theorem 3.2 and noting that $(1 - 2a) > 0$ from Theorem 3.1. Therefore if

$$q_1 \left(\left(1 - 2a\right) q_1 + 2a\right) < 1 \tag{3.16}$$

holds, then inequality (3.9) must also be satisfied. The positive parabola defined by inequality (3.16) has roots $q_{1,+} = 1$ and $q_{1,-} = 2a - 1 < 0$. Namely, if $q_1 < 1$ then the dynamical system is locally asymptotically stable. Moreover, if $q_1 < 1$ then $q_1^2 < 1$, which implies $q_1 q_2 < 1$, thus satisfying the Small Gain theorem (Theorem 2.1). As a special case of Theorem 3.2, if each cell in the cellular domain has no adjacent cell of the same type, namely $n_1 = 0$, then inequality (3.9) is equivalent to the Small Gain theorem, as demonstrated previously for checkerboard patterns using lateral-inhibition models (Figure 2) [18], highlighting applicability of the general form of cellular connectivity define in Section 2.3 to control mechanisms of lateral-inhibition systems.

4. Application: Notch-Delta laminar pattern formation in mammary organoids

To illustrate the results of Section 3, we use the Notch-Delta lateral-inhibition model outlined in Section 2.1 that was recast as an interconnected dynamical system in sections 2.2 - 2.4. Namely, we seek cell-cell signal polarity conditions between luminal and basal cells in the mammary organoid to achieve the experimentally observed laminar pattern formation of Notch in a bilayer of cells (Figure 3b-3d). Specifically, we use the laminar pattern existence and stability signal strength bounds derived in Section 3 to isolate regions of w_1 and w_2 that facilitate the aforementioned Notch patterns in quotient systems representing the family of static regular graphs described in Section 2.2. Furthermore, we validate the analytic regions of w_1 and w_2 using fixed lattice large-scale simulations for each graph (see Appendix A simulation methods). Furthermore, we

then investigate the applicability of our static domain analytical results to dynamic cellular domains using cell-based modelling in 2D and 3D (see Appendix B for a description of the cell-based model methods).

4.1. **Cell-type dependent signal anisotropy regions using a Notch-Delta lateral-inhibition model in static bilayer domains.**

We consider the bilayer cellular domain described by the regular graph $\mathcal{G}$ to be partitioned by cell-type. Namely, let π be an equitable partition of $\mathcal{G}$ such that all basal cells are allocated in $P_1 = P_B$ and luminal cells allocated in $P_2 = P_L$ as in Figure 7a. To apply both Theorem 3.1 and Theorem 3.2 to define signal strength parameter regimes for laminar patterning (Figure 11a), we first explicitly recast the spatially discrete ODE (2.1-2.2) in the form of a quotient SISO system (2.11-2.12). Let $\boldsymbol{x}_i = [N_i, D_i]^T$ denote the vector of state variables of the system, where i designates cellular identity. Then the input to each cell is the local spatial information received via the $\langle\cdot\rangle$ operator, such that $u_i = \langle D_i \rangle = \overline{\boldsymbol{W}}_0 \boldsymbol{D}$. Similarly, the output of each cell is the Delta expression $y_i = D_i$. To apply Theorem 3.1 to our biological model, we need to determine the following: (i) the derivative of the transfer function, T, of the SISO system and (ii) the homogeneous steady state, $\boldsymbol{x}^*$, of the dynamical system.

(i) The derivative of the transfer function can be derived by taking the partial derivative of the SISO system w.r.t. the inputs and state variables, as shown in equation (2.15). Thus, for NDM (2.1-2.2) as presented as an interconnected system in Section 2.4,

$$\frac{\partial h}{\partial \boldsymbol{x}_i} = \begin{bmatrix} 0 & 1 \end{bmatrix}, \quad \frac{\partial \boldsymbol{f}}{\partial \boldsymbol{x}_i} = \begin{bmatrix} -\mu_N & 0 \\ -\frac{bsN_i^{s-1}}{\left(1+bN_i^s\right)^2} & -\mu_D \end{bmatrix} \quad \text{and} \quad \frac{\partial \boldsymbol{f}}{\partial u_i} = \begin{bmatrix} \frac{aru_i^{r-1}}{\left(a+u_i^r\right)^2} \\ 0 \end{bmatrix}. \tag{4.1}$$

Therefore, multiplying the matrices in equation (4.1) and making the substitution $N_i = f(u_i)/\mu_N$ at steady state, yields the following,

$$\begin{aligned} T'(u_i) &= -\begin{bmatrix} 0 & 1 \end{bmatrix} \begin{bmatrix} -\mu_N & 0 \\ -\frac{bsN_i^{s-1}}{\left(1+bN_i^s\right)^2} & -\mu_D \end{bmatrix}^{-1} \begin{bmatrix} \frac{aru_i^{r-1}}{\left(a+u_i^r\right)^2} \\ 0 \end{bmatrix}, \\ &= -\frac{abrs\mu_N^s \left(a+u_i^r\right)^{s-1} u_i^{rs-1}}{\mu_D \left(\mu_N^s \left(a+u_i^r\right) + bu_i^{rs}\right)^2}. \end{aligned} \tag{4.2}$$

(ii) We now solve the NDM (2.1-2.2) for the homogeneous steady state. This problem is reduced to solving $\boldsymbol{f}\left(\boldsymbol{x}^*, D^*\right) = 0$ as $u_i^* = D_i^* = D^*$ for all $i = 1, ..., N$ in the case of a system of identical cells. Solving the system (2.1-2.2) for homogeneous steady states means solving the following polynomial for D^*,

$$b\mu_D \left(D^*\right)^{rs+1} + \mu_N^s \left(\mu_D D^* - 1\right)\left(a + \left(D^*\right)^r\right)^s = 0. \tag{4.3}$$

We choose the parameter values $a = 0.01$, $b = 100$, $\mu_N = \mu_D = 1$, $s = 1$ and $r = 2$ selected previously [10], with the only modification of s to simplify calculations for demonstration purposes. To be able to apply Theorem 3.1, we require that $|T'(u^*)| > 1$ because $w_1 > 0$. This condition is equivalent to the requirement derived by direct linear analysis of a single cell as in [10], where they show that the existence of the homogeneous steady state instability can only occur when

$$f'(u^*)g'(N^*) < -1. \tag{4.4}$$

It can be shown that $T'(u^*) = f'(u^*)g'\left(f\left(u^*\right)/\mu_N\right)/(\mu_N\mu_D)$ for a closed-loop system of two cells [17], then applying the same parameter groupings and values for μ_N and μ_D as in [10] yields the equivalent condition. Moreover, $|T'\left(u^*\right)|$ is a monotone increasing function with respect to r (see Figure 10), hence increasing the nonlinearity of the ODE system relaxes the restrictions on w_1 for the existence of pattern emergence imposed by Theorem 3.1, therefore emphasising the relationship between the connectivity of the cells and the characteristics of the intracellular ODE system.

Solving the cubic polynomial (4.3) when $r = 2$ yields a homogeneous steady state $D^* = 0.049$, therefore, we have both (i) and (ii). Applying Theorem 3.1 to the NDM system (2.1-2.2) using equation (4.2) and D^* yields the following bound on signal strength parameters,

$$w_1 < \alpha \frac{w_2}{R_\tau}, \tag{4.5}$$

for $\alpha = 0.21$, which defines a strict (w_1, w_2) parameter space for the emergence of laminar patterning between layers (region below black line in Figure 11b).

As we have found the necessary bound on w_1 for pattern formation, we now seek to use Theorem 3.2 to impose a sufficient bound on w_1 to ensure laminar pattern stability. To apply Theorem 3.2, we require the $\mathcal{L}_2$-gains for each representative cell at steady state q_B and q_L from P_B and P_L, respectively. By the monotonicity of the NDM system (2.1-2.2) with respect to the cones $K^U = \mathbb{R}_{\geq 0}$, $K^Y = -K^U$ and $K^{\boldsymbol{X}} = \{\boldsymbol{x} \in \mathbb{R}^2 | x_1 \geq 0, x_2 \leq 0\}$ [17], we are able to use the steady state relation (2.20). To determine the $\mathcal{L}_2$-gains, we solve for the heterogeneous steady states $\boldsymbol{x}_B$ and $\boldsymbol{x}_L$, with associated input steady states

$$u_B = \frac{n_1 w_1 D_B + n_2 w_2 D_L}{N_w} \quad \text{and} \quad u_L = \frac{n_1 w_1 D_L + n_2 w_2 D_B}{N_w}, \tag{4.6}$$

then using equation (4.2), $q_B = |T'\left(u_B\right)|$ and $q_L = |T'\left(u_L\right)|$. For each static geometry outlined in Table 1, a parameter sweep of the signal strength parameter space (w_1, w_2) was conducted to highlight regions that satisfy the conditions (i) or (ii) and inequality (3.4) from Theorem 3.2, where the heterogeneous steady

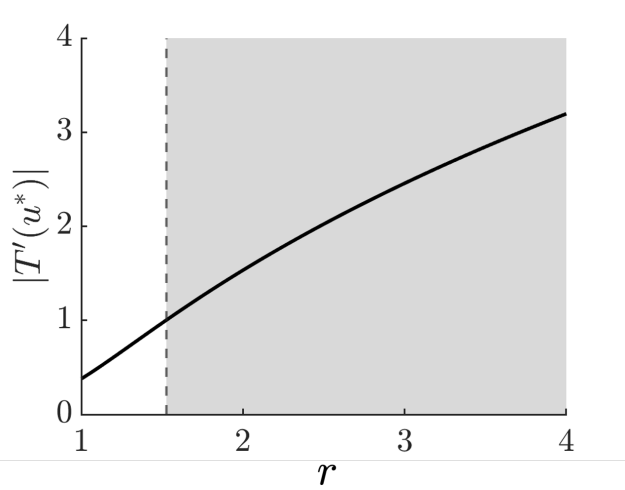

FIGURE 10. Monotonicity $|T'(u^*)|$ with respect to r. Parameter values were chosen as parameter values $a = 0.01$, $b = 100$, $\mu_N = \mu_D = 1$ and $s = 1$. For each r, the homogeneous steady state was solved using equation (4.3). The shaded region represents the values of r that satisfies $|T'(u^*)| > 1$, which is required for the instability of the homogeneous steady state in Theorem 3.1, highlighting a lower bound of $r_{\min} = 1.5$.

states $\boldsymbol{x}_B$ and $\boldsymbol{x}_L$ were numerically solved (see Appendix A). The resulting stability regions in the (w_1, w_2)-space (red shaded regions in Figure 11b) have the same linear form as the analytical existence bound (4.5). Therefore, assuming the same form of relationship between w_1, w_2 and R_τ, a ubiquitous gradient parameter β was extracted from each static lattice parameter sweep. That is, to ensure the local asymptotic stability of the laminar bilayer patterns (Figure 11a) in both 2D and 3D,

$$w_1 < \beta \frac{w_2}{R_\tau} \tag{4.7}$$

must be satisfied, for $\beta = 0.04$. We have provided an improvement on equation (4.5) from necessary to sufficient for laminar pattern formation using the NDM system (2.1-2.2), nevertheless, this defines a highly restrictive parameter bound on w_1 for the given intracellular kinetics parameters, implying that almost all cell-cell signals must be directed towards cells of a different type, emphasising the requirement of apical-basal layer contact.

Finally, using static lattice simulations for each of 2D and 3D geometries described in Table 1 (see Appendix A) we conducted a parameter sweep over the (w_1, w_2)-space to verify the necessary bound of inequality (4.5) and the sufficient bound of inequality (4.7). Namely, the NDM system (2.1-2.2) was numerically solved for each of the connectivity graphs and allowed to converge to steady-state thereby the difference in Notch activation was measured between the layers of cells to verify the existence of laminar patterns. The parameter regions that exhibited the layered patterning using a pattern tolerance of $\delta = 0.1$ (see Appendix A) were consistent with the analytical inequalities (4.5) and (4.7), as demonstrated in Figure 11b by

the blue-shaded regions. Furthermore, the regions defining the observed patterns from numerical simulations had the same linear upper bound for w_1 as a function of w_2 for all 2D and 3D geometries. Therefore, as conducted for the stability inequality (4.7), we extracted a ubiquitous gradient parameter γ. Namely, laminar patterning in a bilayer of cells can be observed if w_1 satisfies,

$$w_1 < \gamma \frac{w_2}{R_\tau} \tag{4.8}$$

where $\gamma = 0.11$. Note that due to the symmetry of the system, that is, each cell has identical internal kinetics that are spatially coupled by a regular and undirected graph, then to achieve the laminar patterning in the correct direction, the system required a small perturbation using initial conditions. Moreover, as the pattern tolerance $\delta \to 0$ (see Appendix A) then $\gamma \to \alpha$, due to the contrast between the layers becoming weaker, see Figure 12b. Thus the arbitrary choice of δ defines what is considered as acceptable patterning, though we note that the necessary bound provided by Theorem 3.1 is always satisfied.

As the observed pattern regions lie within the existence bound regions ($\gamma < \alpha$) and the sufficient stability bound regions are a subset of the observed pattern regions ($\beta < \gamma$) in (w_1, w_2)-space (Figure 11b), we numerically verify the analytical conditions imposed on the signal strength parameters w_1 and w_2 by Theorem 3.1 and Theorem 3.2 using the NDM system (2.1-2.2). In each case, for existence, stability and numerical observation, there exists a consistent form for the upper bound of the cell-type dependent signal strength parameter w_1, which relates cellular connectivity to signal strength polarisation, via R_τ, independent of lattice dimension.

In summary, from the analytic and empirical upper bounds on the homotypic signal strength, w_1, outlined above reveal that the lattice geometries with the low R_τ values require the less active polarisation to generate and maintain laminar patterns. For example, the 2DM lattice (see Table 1) has lowest neighbourhood cell-type ratio with$R_\tau = 2/3$, and therefore has the largest regions in (w_1, w_2)-space for existence, stability and observed laminar patterns (Figures 11b and 11c). In contrast, the 3DVN lattice has the largest R_τ value, thus producing the smallest patterning regions and thus great amounts of polarisation are needed to produce laminar patterns (Figure 11b). These findings highlight that laminar pattern formation using a lateral-inhibition mechanism is highly sensitive neighbourhood composition of the bilayer structure, suggesting that the contrasting phenotypes of the basal and luminal cells (elongated and cuboidal shapes, respectively) may play a significant role in pattern maintenance during mammary development. Though the cell-type composition is an important factor, we found that all 2D and 3D geometries we considered required signal polarisation to achieve laminar patterning, such that $w_1 < w_2$ (Figure 11b), indicating the existence of a polarity mechanism within the intracellular system.

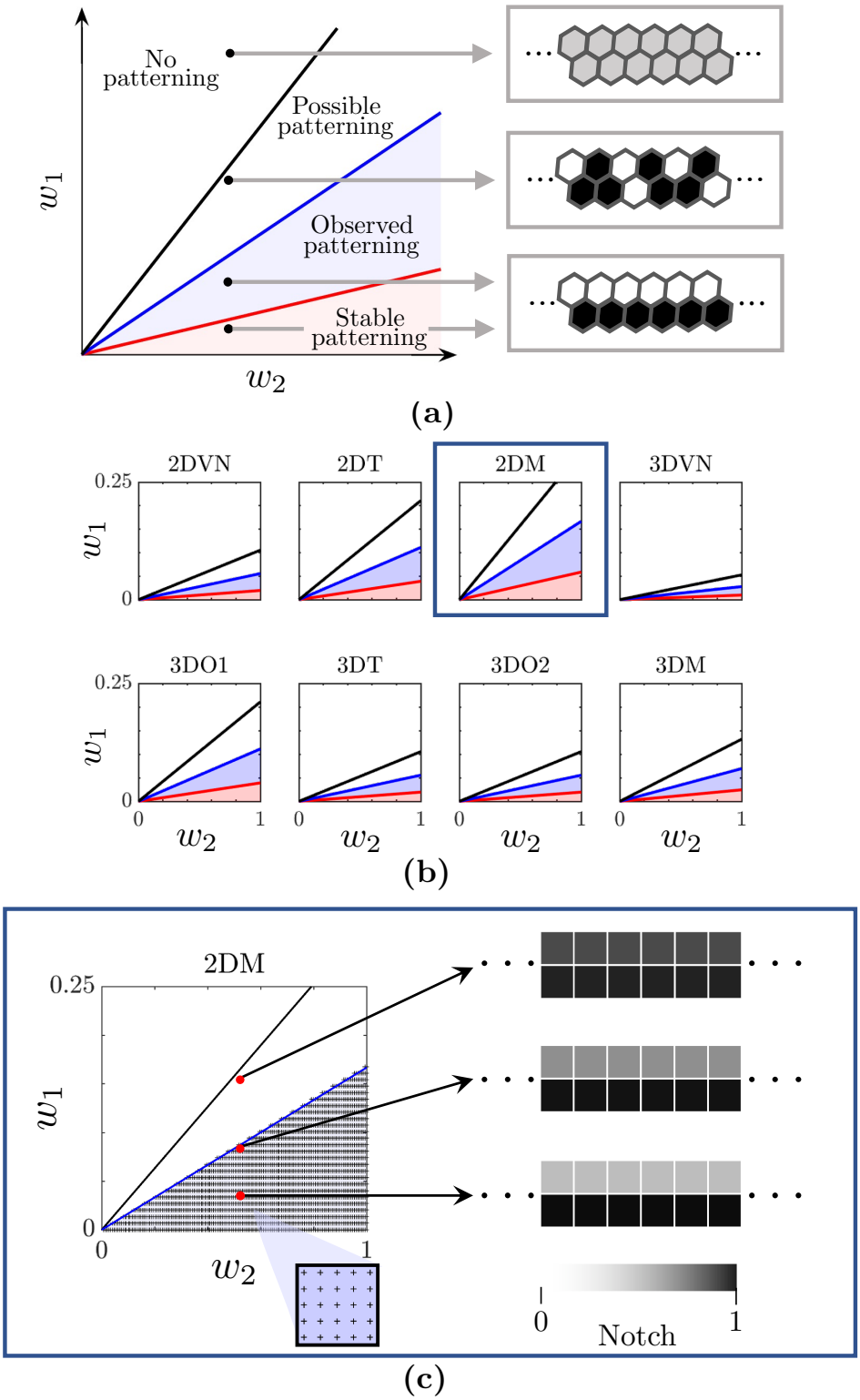

FIGURE 11. Cell-type dependent Signal strength polarisation regions for laminar pattern formation in static bilayer geometries. (a) The left diagram represents the (w_1, w_2) parameter space that yields conditions for bilayer laminar patterning. The region above the black line corresponds to stability of the steady state, where the black line is the upper bound of w_1 provided by inequality (3.1) in Theorem 3.1. (Continued on the following page.)

FIGURE 11. (Continued.) The blue line is the upper bound of w_1 determined from numerical simulations of the ODE system and the red line is the upper bound for analytical stability of the heterogeneous steady states provided by inequality (3.4) in Theorem 3.2. Representative patterns are embedded into the 2D Triangulated lattice. (b) (w_1, w_2) parameter space highlighting laminar pattern regions shown in (a) for each static geometry outlined in Table 1 with example simulation results shown in (c) using the 2DM lattice (highlighted). The magnified region of (w_1, w_2)-space demonstrates the high density of parameter values with the capacity to produce laminar patterning, denoted by $+$, which defines the blue observed regions in all static lattice simulations. Red points represent the parameter values used in the example simulations on the right. (w_1, w_2)-space was discretised into 150×150 regular grid lattice for $w_1 \in (0, 0.25]$ and $w_2 \in (0, 1]$, resulting in 2.25×10^4 simulations per static geometry. For further details on static simulations, see Appendix A.

The graph partitioning methods applied here highlight the flexibility of the cellular domain in pattern formation analysis. Specifically, the only information required is the cell-type neighbourhood composition for any given cells, independent of the physical dimension. Therefore, we propose such a neighbourhood composition sensing mechanism could be used by cells to maintain the observed pattern formation in developing systems where connectivity graphs are not regular and independent on time. That is, adaptive activator ligand membrane localisation is dependent on current neighbours in contact with the cell.

4.2. **Adaptive cell-type dependent signal anisotropy mechanisms using a Notch-Delta lateral-inhibition model in dynamic bilayer domains.**

In section 4.1, analytical and numerical bounds on w_1 were derived for the existence and stability of Notch-Delta polarisation in static bilayer cell domains. Motivated by the consistency of the laminar patterning of Notch in the developing mammary gland (see Figure 3), we seek to test if the static bounds derived on w_1 can produce the same pattern formation in dynamic domains. In addition, we investigate the efficacy of using a fixed and adaptive upper bound of w_1 to ensure laminar pattern stability in bilayers.

We simulate dynamic cellular domains using cell-based modelling such that each cell is represented as a point in space equipped with a connectivity radius that corresponds to the cell membrane. We say that cells are connected if their connectivity regions overlap in space, which generates a connectivity graph as described in Section 2.2. By embedding small amounts of stochastic motion in addition to spring-like mechanical properties to a bilayer of cells, we generate a time-dependent stochastic connectivity network that approximates junction transitions in developing tissues. Furthermore, each node is designated a cell type which allows for the study of cell-type dependent signal edges for stochastic networks when coupled with the NDM intracellular kinetics (2.1-2.2). As in the static geometry investigation, each cell-based simulation is initiated with a bilayer of cells with luminal and basal on the inner and outer surface, respectively, thereby representing the cell structure of the mammary organoid. For further information on the cell-based simulations and NDM (2.1-2.2) integration, see Appendix B.

When transitioning to dynamic domains, we cannot always satisfy the equitable property of the cell-type partitions P_B and P_L in the bilayer connectivity graph due to the absence of regularity. Consequently, the analytical conditions derived in Section 3 cannot be applied at each timestep of the simulations, instead, we use the static domain inequalities (4.7-4.8) to gain an intuition for ligand activator polarisation conditions in dynamic geometries to generate and maintain laminar patterns. In particular, we focus on how a cell responds to the microenvironment via two cell-type signal strength mechanisms: (i) globally fixed values of w_1 and w_2 and (ii) a locally adaptive w_1 for a globally fixed w_2. By investigating these two types of signal strength mechanisms in the dynamic cellular domains, we can measure the influence of varying cellular connections on pattern stability as the system evolves. Specifically, we determine efficacy of both pattern control mechanisms by mean difference in Notch activation between each cell-type, ΔN, and is defined as

$$\Delta N = \frac{1}{\mathcal{N}_L}\sum_{i}^{\mathcal{N}}(1-\delta_{\tau(i),\tau(B)})N_i - \frac{1}{\mathcal{N}_B}\sum_{i}^{\mathcal{N}}\delta_{\tau(i),\tau(B)}N_i, \tag{4.9}$$

where $\mathcal{N}$ is the total number of cells, $\mathcal{N}_L$ is the number of luminal cells and $\mathcal{N}_B$ is the number of basal cells. The function $\delta_{\tau(i),\tau(B)}$ is the cell-type Kronecker delta function,

$$\delta_{\tau(i),\tau(B)} = \begin{cases} 1 & \text{if cell } i \text{ is a basal cell,} \\ 0 & \text{if cell } i \text{ is a luminal cell.} \end{cases} \tag{4.10}$$

Specifically, $\Delta N \approx 1$ implies complete laminar patterns of Notch activation, whereas $\Delta N \approx 0$ is considered as no consistent laminar patterns between the layers of cells.

The *fixed* mechanism for w_1 (case (i)) is used to represent a high inertia of cellular adaptability to the local environment of the cell, that is, that transmission strengths are defined at birth. Here, the w_1 is set to agree with the inequalities (4.7) or (4.8), designated as "Fixed β" (Fβ) or "Fixed γ" (Fγ), respectively. Using the *fixed* mechanism in dynamics simulations, the R_τ value is defined by the initial connectivity of the geometry and is constant throughout the simulation.

The *adaptive* mechanism for w_1 (case (ii)) is used to represent a low inertia of cellular response to the microenviroment. That is, for each cell, w_1 is updated at each timestep to satisfy the observed static inequality (4.8) by determining $R_{\tau,i}$, i.e. the cell-type composition of the neighbourhood for each cell i (see Appendix B). We denote this signal strength mechanism "Adaptive γ" (Aγ).

Simulating each signal strength mechanism, Fβ, Fγ, Aγ for 100 hours highlighted that conditions defining laminar pattern regions in static geometrics, inequalities (4.7) and (4.8), allow for the emergence of laminar patterns in dynamic cell geometries up to small spatial perturbations, Figure 12a. That is, each mechanism initially ($t < 50h$) produced concentric contrasting layers of Notch expression, however, as the bilayer

geometry became deformed due to the random perturbations of each cell, the definition between layers was lost by 100 hours (Figures 12a-12c). Thus, information about cell-type signal polarisation is preserved when partitions of the connected graph are no longer equitable, however, the retained information is insufficient for the long-term stability of the Notch states.

In terms of pattern intensity and retention, using the Fixed β polarisation mechanism performed the best (Figure 12a). Though due to the high contrast between layers, the variance in Notch expression quickly becomes very large once consistent patterning is lost, Figures 12b-12c. The region of (w_1, w_2)-space, defined by inequality (4.7), which is sufficient for stability of heterogeneous states between layers of static bilayers is highly restrictive, such that $w_1 \approx 0$ for all 2D and 3D geometries. In the context of the mammary bilayer, the simulation using Fixed β accounts for the situation of no almost Delta ligands are located on the luminal-luminal and basal-basal interface, again indicating the existence of a Delta inhibition mechanism at these membranes.

The Fixed γ signalling mechanism produced the least contrast of Notch expression between layers initially and was quick to lose the consistency of expression, therefore performing the worst out of the signal strength mechanisms (Figures 12b-12c). However, the Adaptive γ signal strength mechanism yielded the greatest pattern retention over the total time, highlighted by the lowest variance from ΔN values Figures 12b-12c. As Adaptive γ allows for $w_1 \approx \gamma$ (see Figure 12d), this ability of the cell to update signal strength depends on the local cell-type composition, enables cells to still signal to cells of the same type whilst maintaining the concentric patterning. This highlights that if homotypic signalling is observed, then cells may be actively adapting to the microenvironment to stabilise stratification.

Furthermore, using the Adaptive γ signal strength mechanism revealed that there are stricter polarisation conditions in the basal cells than luminal cells while laminar patterning is maintained, for $t < 50$h (Figures 12a-12c). Subsequently, by the inverse relationship between the cell-type connectivity and lateral-inhibition model (Theorem 3.1), the restricted cellular signalling imposed on the basal cells may induce laminar pattern formation within the luminal cells, whilst allowing for greater luminal-luminal cell communication (Figure 12d). Moreover, at $t \approx 50$h, a basal cell was disconnected from the luminal layer, producing a transient irregularity for w_1 values (bounded above by inequality (4.5)), and therefore initiating the deterioration of laminar patterning (Figure 12d.)

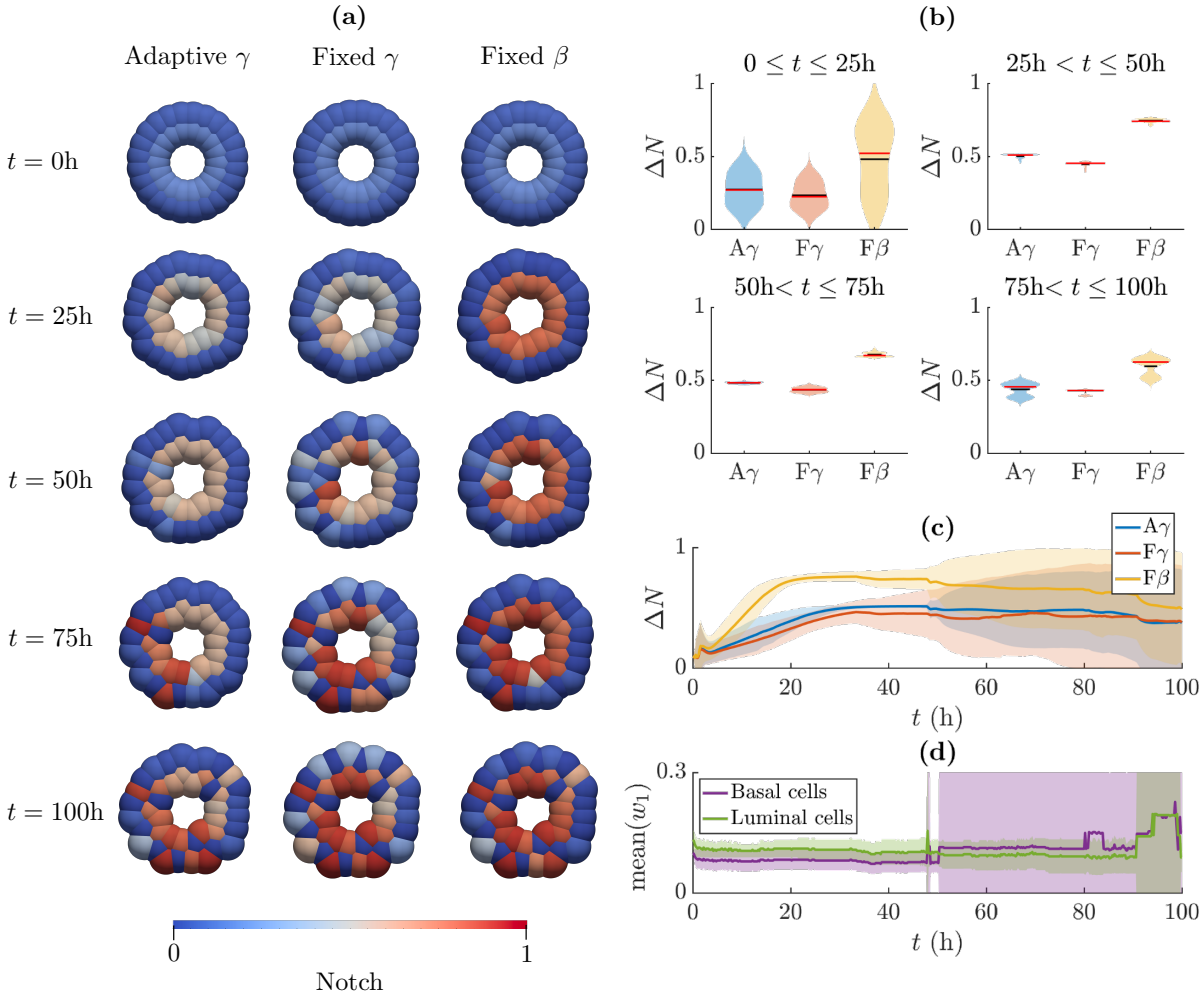

FIGURE 12. 2D dynamic cellular domain simulation results of fixed and adaptive signal strength polarisation with each simulation using a globally fixed value of $w_2 = 1$. (a) Cell-based simulations of a cross-section of a bilayer spheroid. The simulations were run for 100 hours, initialised with cell-type stratification (see Figure 15), and ODE initial conditions $\boldsymbol{x}_B(0) = [0.1, 0.2]^T$ and $\boldsymbol{x}_L(0) = [0.2, 0.1]^T$ for basal and luminal cells, respectively. The colour of each sphere represents the intracellular level of Notch. No noise was introduced to the ODE systems for Notch and Delta dynamics, the variability in these values presented is induced from the small spatial perturbations on each cell. (b) Violin plots summarising the Notch values in (a) over four 25h periods. Shaded regions denote the probability density of the ΔN values over each period. The black and red lines are the means and medians of the ΔN values, respectively. (c) A plot of the ΔN value for each signal polarity mechanism over time. Shaded regions represent standard deviations from the mean Notch expression of each cell type. (d) An additional output plot for the adaptive signalling mechanism demonstrating the disparity of w_1 values for basal and luminal cells over time. Shaded regions represent standard deviations from the mean w_1 of each cell type. For further information on the cell-based model, see Appendix B.

Cell-based simulations investigating the efficacy of the static geometry polarisation conditions in dynamic domains were initially conducted on 2D cross-sections of bilayer spheroids. Analysis conducted on static

geometries suggested that the signal strength conditions on w_1 are independent of the physical dimension. We show in Figures 13a-13b that simulations of 3D spheroids are in agreement with 2D cross-sections, namely, that both the *fixed* and *adaptive* signalling mechanisms are capable of generating laminar patterning but are unable to retain the definition of the layers for long periods. Due to the increase of cells in the 3D simulations, the variance of local connectivities is greater as random motion applied was to each cell at every timestep (see Appendix B). Consequently, the time at which consistent laminar patterning is lost much earlier at $t \approx 20$h (Figure 13b) when using the same parameter values as in the 2D simulations.

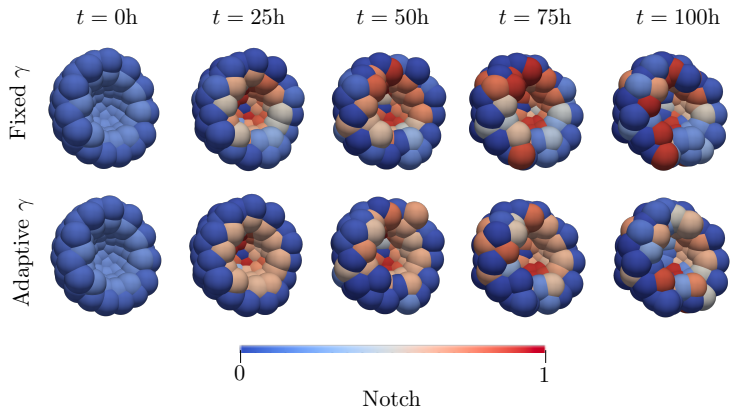

(a)

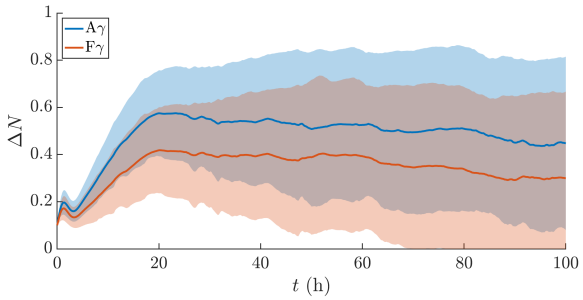

(b)

FIGURE 13. 3D cell-based simulation of a bilayer spheroid representing a developing mammary organoid using examples of the *adaptive* and *fixed* signal strength mechanisms. (a) The simulations were run for 100 hours, initialised with cell-type stratification (see Figure 15b), and ODE initial conditions $\boldsymbol{x}_B(0) = [0.1, 0.2]^T$ and $\boldsymbol{x}_L(0) = [0.2, 0.1]^T$. The colour of each sphere represents the intracellular level of Notch. Only half of the spheroids are visualised to show the dynamics of the internal luminal cells. (b) A plot of the ΔN value for both Fixed γ and Adaptive γ signal polarity mechanisms over time for the 3D simulations. Shaded regions represent standard deviations from the mean Notch expression of each cell-type.

We note that initial spatial conditions are not identical as in the 2D simulations as currently there exists no solution to map equidistant points that cover the surface of a sphere [37]. We instead use the Fibonacci spiral method as an approximate solution, though, this produces clustering of cells at the poles of the sphere

[38], and so introduces initial artefacts to cellular connectivity in the simulations which is a possible cause of the reduced time to pattern degradation.

5. Discussion

We have developed a framework for investigating cell-type dependent juxtacrine signal strength polarisation conditions for emergence and stability of laminar patterning in symmetric bilayer structures via lateral-inhibition. Leveraging previous results of graph partitioning on monolayers, we show how the geometry of the cellular domain has a large impact on the capacity of the system to produce heterogeneity. Moreover, using this framework, we replace the algebraically demanding process of linear analysis of large multicellular systems with an exploitation of the spectral properties of the quotient graphs, therefore addressing the complexity issue discussed in previous juxtacrine pattern analysis studies [31].

In Section 3, we provide necessary and sufficient conditions for the existence of laminar patterns in a bilayer of cells. Both existence and stability inequalities (3.1) and (3.4) highlight that increasing connectivity with opposing cell-types allows for larger existence and stability regions in signal strength (w_1, w_2)-space. In the context of a bilayer of cells, as global concavity of the structure increases, luminal cells have a greater probability to connect with more basal cells, thereby relaxing the existence and stability conditions imposed by Theorem 3.1 and Theorem 3.2 by decreasing R_τ. However, this would violate the symmetry between partitions required to apply both Theorem 3.1 and Theorem 3.2, hence we propose investigating asymmetric connections between layers of cells may allow for a relationship between global curvature of the cellular structure and pattern stability. Specifically, allowing the global connectivity graph to be semi-regular such that each of the basal and luminal subpopulations retain regular edge structure, though these structures may differ between the partitions. Subsequently, the semi-regular structures conform with the equitable partition requirement, thus enabling the analytical study of laminar pattern formation with more authentic cell-cell interactions, i.e. preserving phenotypes and subpopulation sizes.

In addition, as the signal polarisation constraints, inequalities (3.1) and (3.4), are independent of the lateral-inhibition model, Theorem 3.1 emphasises the influence of connectivity on pattern formation by requiring cell-type signal strength heterogeneity. Therefore, in cell-type stratified bilayer geometries such as those seen in Figure 5, cell-type dependent signal strength polarisation is required for the existence of heterogeneous steady states, which is independent of the precise intracellular kinetics of the Notch pathway in the mammary organoid. This indicates the critical role of cellular connectivity in juxtacrine systems as initially highlighted in [12] and thus the geometry of the cellular domain should be carefully considered in fine-grain pattern analysis.

By studying a family of 2D and 3D static cellular domains of varying connectivity, we gain insight into the emergence and stability of concentric layer pattern formation in dynamic domains. Namely, by employing the bounds on w_1 derived from the static simulations, we were able to generate the laminar patterns in 2D and 3D bilayer spheroids when imposing random spatial perturbations on each cell. However, these patterns become unstable as geometry deformation increases, producing disorganised layers of Notch expression even when using an adaptive polarisation mechanism (Figure 12 and Figure 13). Therefore, the information obtained from static domains is insufficient to fully characterise the behaviour of the lateral-inhibition model in a developing mammary organoid.

In this study we assume that the laminar pattern formation is driven purely by signal strength polarisation between the layers, thus neglecting the effect of the external environment on the biological system. That is, we neglect the influence of stroma or extracellular matrix and the importance of the lumen to the luminal cells in supporting the high contrast of Notch expression *in vivo* and *in vitro*, respectively [22]. Thus, applying supplementary boundary conditions in dynamic domains in addition to signal polarisation may achieve laminar patterning, invariant to morphological perturbations.

Furthermore, we note that the parameters chosen for the cell-based simulations were selected to preserve a bilayer structure while perturbing the neighbourhood composition of each cell. Consequently, in Section 4.2 we highlight the sensitivity of our pattern analysis methods to the mechanical properties of the cells, specifically in the instance of a bilayer disconnect resulting in sudden dissipation of laminar patterns (Figure 12). As cell-based models were used to demonstrate the limitations of static pattern analysis of developing systems, more appropriate methods of neighbourhood composition perturbations, such as stochastic edge structure in fixed vertex networks, should be employed to rigorously analyse the effect of cell-type composition fluctuations on global pattern convergence and the development of pattern control mechanisms [39].

Applying the analytical polarisation conditions of Theorem 3.1 and Theorem 3.2 to the context of a mammary organoid using the Collier et al. (1996) NDM we revealed that if patterns are to be experimentally observed then we require almost no juxtacrine communication between cells within the same layer. A plausible process to address the polarisation of Notch activators may involve Cadherins [40], which are transmembrane proteins that mediate cell-cell adhesions. Differential expression of cadherins (E-cadherins are associated with luminal cells and P-cadherins are associated with the basal cells) are suggested to promote self-organisation to form bilayer structures in the mammary gland via cellular affinity to homophilic interactions [40]. There is growing evidence for an inverse relationship between Notch and E-cadherins in biological systems, including mammary epithelia [41–43]. In addition, it has been verified that E-cadherins located between luminal cells promote lumen formation during mammary organoid development [44]. Therefore, we propose that there

exists a Cadherin adhesion-dependent Notch inhibition mechanism that promotes the localisation of Delta ligands on the luminal-basal interface (Figure 14).

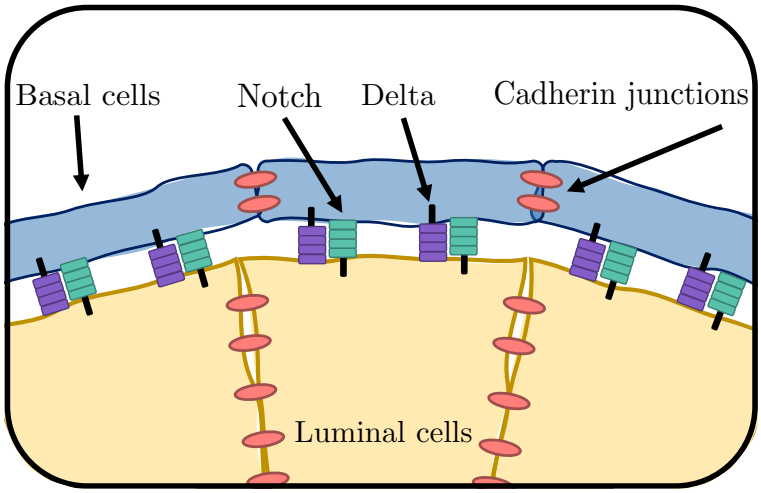

FIGURE 14. Proposed spatial distribution of Notch, Delta and Cadherin junctions within a developing mammary organoid. Due to the adhesion required to maintain the bilayer structure with a hollow lumen, tight junctions form, inhibiting the function of the membrane-bound Notch receptors and Delta ligands between cells in the same layers.

ACKNOWLEDGEMENTS

JWM is supported by Knowledge Economy Skills Scholarships (KESS2), a pan-Wales higher-level skills initiative led by Bangor University on behalf of the Higher Education sector in Wales. It is part-funded by the Welsh Government's European Social Fund (ESF).

SUPPORTING INFORMATION

Source code for both dynamic and static lattice simulations can be found at `http://bit.ly/Bilayer_sims_repo`.

REFERENCES

[1] S. F. Gilbert, *Developmental biology*, ch. 6. Sinauer Associates Inc, eleventh edition. ed., 2016.

[2] R. Cagan, "Principles of drosophila eye differentiation," *Current topics in developmental biology*, vol. 89, pp. 115–135, 2009.

[3] H. Togashi, K. Kominami, M. Waseda, H. Komura, J. Miyoshi, M. Takeichi, and Y. Takai, "Nectins establish a checkerboard-like cellular pattern in the auditory epithelium," *Science*, vol. 333, pp. 1144–1147, 2011.

[4] H. Kim, L. Huang, P. J. Critser, Z. Yang, R. J. Chan, L. Wang, S. L. Voytik-Harbin, I. D. Bernstein, and M. C. Yoder, "Notch ligand delta-like 1 promotes in vivo vasculogenesis in human cord blood–derived endothelial colony forming cells," *Cytotherapy*, vol. 17, pp. 579–592, 2015.

[5] A. M. Turing, "The chemical basis of morphogenesis," *Philosophical Transactions of the Royal Society of London. Series B, Biological Sciences*, vol. 237, no. 641, pp. 37–72, 1952.

[6] T. E. Woolley, R. E. Baker, and P. K. Maini, "Turing's theory of morphogenesis: where we started, where we are and where we want to go," in *The incomputable*, pp. 219–235, Springer, 2017.

[7] Z. Hadjivasiliou, G. L. Hunter, and B. Baum, "A new mechanism for spatial pattern formation via lateral and protrusionmediated lateral signalling," *Journal of the Royal Society Interface*, vol. 13, 2016.

[8] B. N. Manz and J. T. Groves, "Spatial organization and signal transduction at intercellular junctions," *Nature Reviews Molecular Cell Biology*, vol. 11, pp. 342–352, 2010.

[9] S. J. Bray, "Notch signalling: A simple pathway becomes complex," *Nature Reviews Molecular Cell Biology*, vol. 7, pp. 678–689, 2006.

[10] J. R. Collier, N. A. Monk, P. K. Maini, and J. H. Lewis, "Pattern formation by lateral inhibition with feedback: A mathematical model of delta-notch intercellular signalling," *Journal of Theoretical Biology*, 1996.

[11] H. J. Wearing and J. A. Sherratt, "Nonlinear analysis of juxtacrine patterns," *SIAM Journal on Applied Mathematics*, vol. 62, pp. 283–309, 2001.

[12] S. D. Webb and M. R. Owen, "Oscillations and patterns in spatially discrete models for developmental intercellular signalling," *Journal of Mathematical Biology*, vol. 48, pp. 444–476, 2004.

[13] S. D. Webb and M. R. Owen, "Intra-membrane ligand diffusion and cell shape modulate juxtacrine patterning," *Journal of Theoretical Biology*, vol. 230, pp. 99–117, 2004.

[14] P. Formosa-Jordan and M. Ibañes, "Competition in notch signaling with cis enriches cell fate decisions," *PLoS ONE*, vol. 9, 2014.

[15] A. M. Lilja, V. Rodilla, M. Huyghe, E. Hannezo, C. Landragin, O. Renaud, O. Leroy, S. Rulands, B. D. Simons, and S. Fre, "Clonal analysis of notch1-expressing cells reveals the existence of unipotent stem cells that retain long-term plasticity in the embryonic mammary gland," *Nature Cell Biology*, vol. 20, pp. 677–687, 2018.

[16] H. Hamada, M. Watanabe, H. E. Lau, T. Nishida, T. Hasegawa, D. M. Parichy, and S. Kondo, "Involvement of delta/notch signaling in zebrafish adult pigment stripe patterning," *Development*, vol. 141, pp. 318–324, 2014.

[17] M. Arcak, "Pattern formation by lateral inhibition in large-scale networks of cells," *IEEE Transactions on Automatic Control*, vol. 58, pp. 1250–1262, 2013.

[18] A. S. Rufino Ferreira and M. Arcak, "Graph partitioning approach to predicting patterns in lateral inhibition systems," *SIAM Journal on Applied Dynamical Systems*, vol. 12, pp. 2012–2031, 2013.

[19] M. C. Jørgensen, K. H. de Lichtenberg, C. A. Collin, R. Klinck, J. H. Ekberg, M. S. Engelstoft, H. Lickert, and P. Serup, "Neurog3-dependent pancreas dysgenesis causes ectopic pancreas in hes1 mutant mice," *Development (Cambridge)*, vol. 145, pp. 1–11, 2018.

[20] S. Fre, M. Huyghe, P. Mourikis, S. Robine, D. Louvard, and S. Artavanis-Tsakonas, "Notch signals control the fate of immature progenitor cells in the intestine," *Nature*, vol. 435, no. 7044, pp. 964–968, 2005.

[21] D. Lafkas, A. Shelton, C. Chiu, G. De Leon Boenig, Y. Chen, S. S. Stawicki, C. Siltanen, M. Reichelt, M. Zhou, X. Wu, J. Eastham-Anderson, H. Moore, M. Roose-Girma, Y. Chinn, J. Q. Hang, S. Warming, J. Egen, W. P. Lee, C. Austin, Y. Wu, J. Payandeh, J. B. Lowe, and C. W. Siebel, "Therapeutic antibodies reveal notch control of transdifferentiation in the adult lung," *Nature*, vol. 528, pp. 127–131, 2015.

[22] B. Lloyd-Lewis, P. Mourikis, and S. Fre, "Notch signalling: sensor and instructor of the microenvironment to coordinate cell fate and organ morphogenesis," *Current Opinion in Cell Biology*, vol. 61, pp. 16–23, 2019.

[23] M. Simian and M. J. Bissell, "Organoids: A historical perspective of thinking in three dimensions," *Journal of Cell Biology*, vol. 216, pp. 31–40, 2017.

[24] T. Bouras, B. Pal, F. Vaillant, G. Harburg, M. L. Asselin-Labat, S. R. Oakes, G. J. Lindeman, and J. E. Visvader, "Notch signaling regulates mammary stem cell function and luminal cell-fate commitment," *Cell Stem Cell*, vol. 3, pp. 429–441, 2008.

[25] D. Lafkas, V. Rodilla, M. Huyghe, L. Mourao, H. Kiaris, and S. Fre, "Notch3 marks clonogenic mammary luminal progenitor cells in vivo," *Journal of Cell Biology*, vol. 203, pp. 47–56, 2013.

[26] W. Hordjik, "An overview of computation in cellular automata," *Phys Comp*, vol. 96, pp. 1–10, 1996.

[27] T. Toffoli and N. Margolus, *Cellular automata machines: a new environment for modeling*, ch. 5, pp. 60–65. MIT press, 1987.

[28] B. Bollobás, *Modern graph theory*, vol. 184, ch. 1. Springer Science & Business Media, 2013.

[29] C. D. Godsil, "Compact graphs and equitable partitions," *Linear Algebra and Its Applications*, vol. 255, pp. 259–266, 1997.

[30] D. Angeli and E. D. Sontag, *Interconnections of Monotone Systems with Steady-State Characteristics*, pp. 135–154. 2004.

[31] H. J. Wearing, M. R. Owen, and J. A. Sherratt, "Mathematical modelling of juxtacrine patterning," *Bulletin of Mathematical Biology*, vol. 62, pp. 293–320, 2000.

[32] D. Angeli and E. D. Sontag, "Monotone control systems," *IEEE Transactions on Automatic Control*, vol. 48, pp. 1684–1698, 2003.

[33] A. J. van der Schaft, $\mathcal{L}_2$ *Gain and Passivity Techniques in Nonlinear Control*, ch. 1. 1996.

[34] D. Angeli and E. D. Sontag, "Multi-stability in monotone input/output systems," *Systems & Control Letters*, vol. 51, no. 3-4, pp. 185–202, 2004.

[35] K. C. Chang, K. Pearson, and T. Zhang, "Perron-frobenius theorem for nonnegative tensors," *Communications in Mathematical Sciences*, vol. 6, pp. 507–520, 2008.

[36] W. M. Haddad and V. Chellaboina, *Nonlinear dynamical systems and control: a Lyapunov-based approach*. Princeton university press, 2011.

[37] A. Araújo and P. Serranho, "On the use of quasi-equidistant source points over the sphere surface for the method of fundamental solutions," *Journal of Computational and Applied Mathematics*, vol. 359, pp. 55–68, 2019.

[38] Á. González, "Measurement of areas on a sphere using fibonacci and latitude-longitude lattices," *Mathematical Geosciences*, vol. 42, p. 49, 2010.

[39] X. Zhai, W. Zhou, G. Fei, C. Lu, S. Wen, and G. Hu, "Edge-based stochastic network model reveals structural complexity of edges," *Future Generation Computer Systems*, vol. 100, pp. 1073–1087, 2019.

[40] K. A. Knudsen and M. J. Wheelock, "Cadherins and the mammary gland," *Journal of Cellular Biochemistry*, vol. 95, pp. 488–496, 2005.

[41] P. S. Pereira, A. Teixeira, S. Pinho, P. Ferreira, J. Fernandes, C. Oliveira, R. Seruca, G. Suriano, and F. Casares, "E-cadherin missense mutations, associated with hereditary diffuse gastric cancer (hdgc) syndrome, display distinct invasive behaviors and genetic interactions with the wnt and notch pathways in drosophila epithelia," *Human Molecular Genetics*, vol. 15, pp. 1704–1712, 2006.

[42] K. G. Leong, K. Niessen, I. Kulic, A. Raouf, C. Eaves, I. Pollet, and A. Karsan, "Jagged1-mediated notch activation induces epithelial-to-mesenchymal transition through slug-induced repression of e-cadherin," *Journal of Experimental Medicine*, vol. 204, pp. 2935–2948, 2007.

[43] J. Chen, N. Imanaka, and J. D. Griffin, "Hypoxia potentiates notch signaling in breast cancer leading to decreased e-cadherin expression and increased cell migration and invasion," *British journal of cancer*, vol. 102, pp. 351–360, 2010.

[44] E. R. Shamir, E. Pappalardo, D. M. Jorgens, K. Coutinho, W. T. Tsai, K. Aziz, M. Auer, P. T. Tran, J. S. Bader, and A. J. Ewald, "Twist1-induced dissemination preserves epithelial identity and requires e-cadherin," *Journal of Cell Biology*, vol. 204, pp. 839–856, 2014.

[45] G. R. Mirams, C. J. Arthurs, M. O. Bernabeu, R. Bordas, J. Cooper, A. Corrias, Y. Davit, S. J. Dunn, A. G. Fletcher, D. G. Harvey, M. E. Marsh, J. M. Osborne, P. Pathmanathan, J. Pitt-Francis,

J. Southern, N. Zemzemi, and D. J. Gavaghan, "Chaste: An open source c++ library for computational physiology and biology," *PLoS Computational Biology*, vol. 9, p. e1002970, 2013.

[46] J. M. Osborne, A. G. Fletcher, J. M. Pitt-Francis, P. K. Maini, and D. J. Gavaghan, "Comparing individual-based approaches to modelling the self-organization of multicellular tissues," *PLOS Computational Biology*, vol. 13, p. e1005387, 2017.

[47] K. Atwell, Z. Qin, D. Gavaghan, H. Kugler, E. J. A. Hubbard, and J. M. Osborne, "Mechano-logical model of c. elegans germ line suggests feedback on the cell cycle," *Development (Cambridge)*, vol. 142, no. 22, pp. 3902–3911, 2015.

[48] E. M. Purcell, "Life at low reynolds number," *American journal of physics*, vol. 45, pp. 3–11, 1977.

[49] S. C. Chapra, *Applied numerical methods with MATLAB for engineers and scientists*, ch. 23, pp. 555–572. New York: McGraw-Hill, 2012.

[50] P. Pathmanathan, J. Cooper, A. G. Fletcher, G. R. Mirams, P. K. Murray, J. M. Osborne, J. Pitt-Francis, and J. S. Walter, Alex .and Chapman, "A computational study of discrete mechanical tissue models," *Physical biology*, vol. 6, p. 036001, 2009.

Appendix A. Methods for static lattice simulations

The 2D fixed lattice geometries were considered as a 6 cell system, split equally as luminal and basal cells as demonstrated in Figure 5a. This cyclic geometry generates a system of 12 ODEs that were coupled via the *scaled adjacency matrix* $(1/N_w)\boldsymbol{W}$ as previously discussed in Section 2.2. Similarly, 3D fixed geometries were treated as a cyclic 18 cell system and therefore producing a system of 36 ODEs. For both 2D and 3D geometries, the ODE systems were solved numerically using the `ode45` function in Matlab 2019b. The simulations were solved for 100 hours. If all solutions varied less than 1×10^{-4} over four consecutive iterations, then we assume that the system was considered to have converged to a steady-state. We note that all simulations presented in this study satisfied the convergence criteria.

To determine if the luminal and basal layers have converged to contrasting states of Notch-Delta expression, the mean value of Delta expression was taken from each layer of cells. Explicitly, let d_j denote the mean final Delta values in each layer of cells, such that,

$$d_j = \frac{2}{\mathcal{N}} \sum_{i}^{\mathcal{N}} D_{i,j}, \tag{A.1}$$

where $\mathcal{N}$ is the total number of cells in the system. The difference $\Delta d = |d_1 - d_2|$ indicates the existence of laminar bilayer pattern formation. Note that using Notch as the pattern indicator variable has an identical effect due to the inverse relationship of Notch and Delta. We considered the system to have achieved a laminar bilayer pattern if Δd was greater than a prescribed tolerance, $\delta > 0$.

The static simulation parameter sweeps for w_1 and w_2 where conducted over a discretised 150×150 regular grid lattice for $w_1 \in (0, 0.25]$ and $w_2 \in (0, 1]$, resulting in 22500 simulations per static geometry. In all static lattice simulations, we choose $a = 0.01$, $b = 100$, $\mu_N = \mu_D = 1$, $s = 1$ and $r = 2$ as parameter values for the NDM (2.1-2.2), as previously defined [10].

Appendix B. Methods for lattice free simulations using a cell-based model

Cell-based simulations were carried out using Chaste v2019.1 (Cancer, Heart and Soft Tissue Environment) [45], where the Overlapping Spheres (OS) framework was used to enable seamless transition between 2D and 3D geometries. In addition, it has been previously demonstrated that OS models are highly applicable to study short ranged signal-reaction networks in cellular systems due to the mechanical methods used to define cellular contact [46]. Cells are connected by a mechanical force which is proportional to the region of overlap of spheres defined around each cellular node, see Figure 15. Here, we used the OS force model as defined in [47], where, the displacement of two nodes representing cell centres is represented by the vector $\boldsymbol{r}_{ij} = \boldsymbol{r}_i - \boldsymbol{r}_j$ and the force between the cells is defined by,

$$\boldsymbol{F}_{ij}(t) = \begin{cases} \eta_{ij} s_{ij}(t) \hat{\boldsymbol{r}}_{ij}(t) \log\left(1 + \frac{||\boldsymbol{r}_{ij}(t)|| - s_{ij}(t)}{s_{ij}(t)}\right), & \text{for} \quad ||\boldsymbol{r}_{ij}(t)|| < s_{ij}(t), \\ \eta_{ij} \left(||\boldsymbol{r}_{ij}(t)|| - s_{ij}(t)\right) \hat{\boldsymbol{r}}_{ij}(t) \exp\left(-k_c \frac{||\boldsymbol{r}_{ij}(t)|| - s_{ij}(t)}{s_{ij}(t)}\right), & \text{for} \quad s_{ij}(t) \leq ||\boldsymbol{r}_{ij}(t)|| < r_{\max}, \\ 0, & \text{for} \quad ||\boldsymbol{r}_{ij}(t)|| > r_{\max}, \end{cases} \tag{B.1}$$

where $\eta_{ij}, s_{ij}(t) > 0$ are the spring constant and rest length between cells i and j. $\hat{\boldsymbol{r}}_{ij}(t)$ corresponds to the unit vector of $\boldsymbol{r}_{ij}(t)$ and k_c defines the decay of force between the cells. Upon cellular division, the rest length $s_{ij}(t)$ of both parent and daughter cells are set to $s_{ij}^{\text{div}} = s_{ij}(t)/2$ and will tend back to $s_{ij}(t)$ in finite time as the cell grows. In all simulations, random motion was introduced to each cell to stimulate a dynamic cellular domain. The random motion was implemented by an additional force acting on each cell node at each timestep,

$$\boldsymbol{F}^{\text{rand}} = \sqrt{\frac{2\xi}{\Delta t}} \boldsymbol{\nu}, \tag{B.2}$$

where ξ is a constant defining the size of random perturbation, $\boldsymbol{\nu}$ is a vector of samples from a standard multivariate normal distribution and Δt the timestep of the simulation, as previously defined [46]. The resultant force acting on cell i is defined by,

$$\boldsymbol{F}_i^{\text{res}}(t) = \boldsymbol{F}_i^{\text{rand}} + \sum_j^{\mathcal{N}_i} \boldsymbol{F}_{ij}(t), \tag{B.3}$$

for $\mathcal{N}_i$ is the number of cells within the cut-off distance, $r_{\max}$. Using this resultant force acting upon each cell, we relate this to cellular movement using the assumption that the inertia terms are small in comparison to

the dissipative terms acting upon the cell. This is because both *in vivo* and *in vitro* cells move in dissipative environments with small Reynolds number [48], thus the position of each cell is governed in the Aristotelian regime, such that the velocity of a cell is proportional to the force acting on it. Namely, the spatial dynamics of each cell is determined by,

$$\nu \frac{d\boldsymbol{r}_i}{dt} = \boldsymbol{F}_i^{\text{res}}(t), \tag{B.4}$$

where $\nu > 0$ denotes the damping constant of the spring force. Equation (B.4) is solved using the simple forward Euler method to determine the location of each cell at each timestep, Δt, see Table 2 [49].

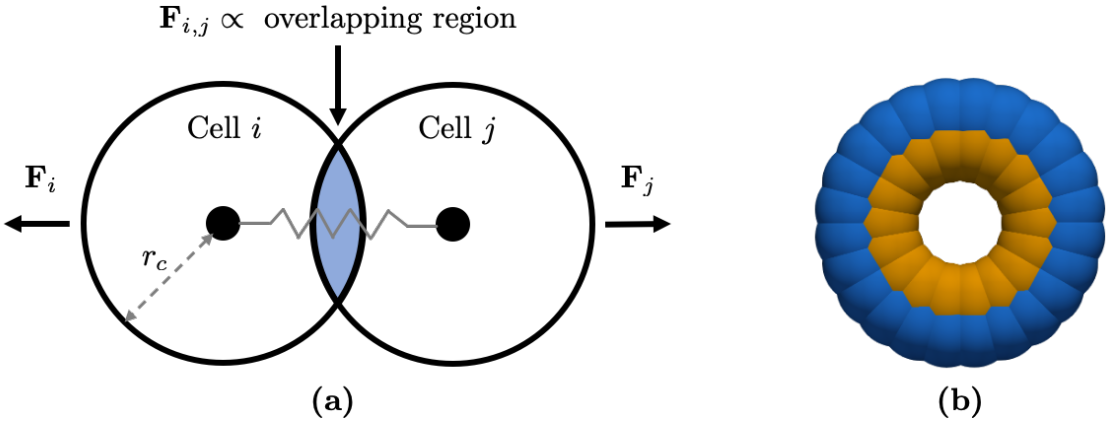

FIGURE 15. The cell-based model using the Overlapping Spheres framework. (a) A schematic of the mechanical dynamics that determines the motion of a cell using the Overlapping Spheres framework. The mechanical force acting on each cell is proportional to the region of overlapped space between any two nodes which are the centre of spheres with radius r_c. The mechanical force between cells i and j can be interpreted as a spring force and due to the relevantly low viscosity of the medium, it is assumed that the motion of each cell is governed in an Aristotelian regime, that is, the force is directly proportional to the velocity of the cell. (b) An example of the 2D initial spatial conditions when simulating the bilayer spheroid. The colours of the cells denote cell types, where the blue and orange cells are the basal and luminal cells respectively. The present example has a spheroid radius of 3 cell diameters (CD).

Simulations were initialised with a bilayer structure, see Figure 15b. Basal and luminal cell types were considered to be mechanically identical to isolate the effects of neighbourhood cell-type composition on Delta patterning. Cells were assumed to not proliferate in both 2D and 3D simulations, this was done to control the spatial organisation of cell types in each layer.

The NDM (2.1-2.2) was integrated into each cell in the population and was solved using the explicit Runge-Kutta45 method [49], which is built into the Chaste software. At every timestep, each cell would sweep through the population to determine the connectivity neighbourhood, which is defined by all nodes within a radius of ρ_c, as in the fixed geometry simulations. In the simulations presented here, we assume the connectivity radius, ρ_c, is equal to the mechanical cut-off length, $r_{\max}$. Once a cellular neighbourhood has been determined for each cell, the average Delta is calculated using equation (2.7), and then updated in the

state variables to be used to solve the next timestep of the NDM (2.1-2.2). In all dynamic lattice simulations, we choose $a = 0.01$, $b = 100$, $\mu_N = \mu_D = 1$, $s = 1$ and $r = 2$ as parameter values for the NDM (2.1-2.2), as previously defined [10].

The seeds used to initialise the generation of the pseudo-random numbers were fixed for all simulations to compare signal strength parameters on dynamic domains. In addition, $w_2 = 1$ was fixed for each comparison simulation. Parameter values used in all cell-based simulations can be found in Table 2.

Parameter	Description	Value	Units	Reference
t_{tot}	Total simulation time	100	h	-
Δt	Timestep	0.01	h	-
η_{ij}	Spring constant	25^*	NCD^{-1}	-
s_{ij}	Spring rest length	1	CD	-
$r_{\max}$	Force cut-off length	$3/2^*$	CD	-
k_c	Decay of force	5	*Dim'less*	[47]
ξ	Random motion perturbation	0.0025^*	*Dim'less*	-
ν	Damping constant	1	NhCD^{-1}	[50]

TABLE 2. Table of parameters used in each cell-based simulation. The unit of length CD refers to the fixed cell diameter used in simulations. * indicates parameter values tuned for bilayer structure maintenance, the rest of the simulation parameters used in this study were extracted from [46].